Mon. Not. R. Astron. Soc. **000**, 1–20 (2011) Printed 5 November 2014 (MN LaTeX style file v2.2)

The origin of the frequency-dependent behaviour of pulsar radio profiles

J. Dyks & B. Rudak
Nicolaus Copernicus Astronomical Center, Rabiańska 8, 87-100, Toruń, Poland⋆

arXiv:1411.0866v1 [astro-ph.SR] 4 Nov 2014

Originally drafted 2014 07 07

ABSTRACT

We present further development of a pulsar emission model based on multiple streams diverging away from the magnetic dipole axis, and forming azimuthally-structured fan-shaped beams. It is shown that this geometry, successfully tested on profiles with bifurcated features, naturally solves several classical pulsar problems and avoids some difficulties of the traditional nested cone/core model. This is best visible for profiles with several components, such as those of class T, Q and M, because they most clearly exhibit a range of effects previously interpreted within the conal model. In particular, with no reference to the flaring boundary of the polar magnetic flux tube, the stream model explains the apparent radius-to-frequency mapping (RFM), including its reduced strength for the inner pair of components. The lag of the central component (apparent 'core') with respect to the centroids of the flanking ('conal') components can also be naturally explained with no reference to emission rings located at disparate altitudes. The stream model also reveals why the millisecond pulsars, despite their more strongly flaring magnetic field lines, do not exhibit as strong RFM as the normal pulsars. The model is then successful in reproducing properties of so disparate objects as the M-class and millisecond pulsars, including some peculiarities of the latter. With no hesitation we, therefore, advance the view that pulsars have fan beams generated by outflowing streams, whereas the nested cone/core beams may well not exist at all.

Key words: pulsars: general – pulsars: individual: B0329+54 – Radiation mechanisms: non-thermal.

1 INTRODUCTION

The first mention of streams we are aware of was that of Michel (1987). The main observational evidence on which he based his idea was the sign reversal of circular polarisation at peaks of components in radio profiles. However, a detectable sign reversal could also be expected for other geometries of the beam, eg. the patchy beam (Lyne & Manchester 1988; Manchester 2012) and the conal one (Rankin 1983), especially if the latter is structured as the 'patchy conal ring' in Fig. 1 of Karastergiou & Johnston (2007). A carefull recent study of the sign reversing circular polarisation is presented in Gangadhara (2010), Wang et al. (2012), and Wang et al. (2010). Moreover, Michel's fan beams were very elongated ($\Delta\theta \sim 1$ rad), and more complicated than the single-parameter conal beams, which seemed to be so well designed to match the imposing flaring polar tube. They were also less attractive, with little inherent symmetry which could automatically explain the approximate left-right symmetry of some pulsar profiles (notably of Q and M class in the classification scheme of Rankin 1983). This may be why Michel's model was not recognised as a promising way to interpet radio pulsar profiles and have in principle been ignored afterwards.

A major development of the stream-based (or fan beam) model has recently been sparked by the properties of bifurcated features residing in pulsar profiles (Dyks et al. 2010a, hereafter DRD10; Dyks & Rudak 2012, hereafter DR12). DRD10 have shown that double notches (McLaughlin & Rankin 2004; Navarro et al. 1997; Rankin & Rathnasree 1997) can be understood in a natural way, if the elementary emitting unit has the form of an elongated stream emitting a bifurcated beam. This model required that both emitting streams and obscuring streams exist in pulsar magnetosphere. The former ones were immediately identified as the *apparently* conal components in the profile of PSR J0437−4715, and the bifurcated precursors in PSR J1012+5307. The bifurcation of a seemingly 'conal' component in PSR J0437−4715, and the fixed (frequency-independent) location of the 'conal' components and notches have suggested that all these features are produced by

⋆ jinx@ncac.torun.pl

© 2011 RAS

a cut of sightline through narrow fan beams emitted by azimuthally-narrow streams.

A change of the peak-to-peak separation between components observed at different frequency ν, and the associated change of pulse profile width, can be interpreted in terms of the radius-to-frequency mapping (RFM, Komesaroff 1970; Cordes 1978). According to the RFM model, the low-ν radiation is emitted at a larger radial distance r, measured from the neutron star centre, than the high-ν radiation. However, the RFM acronym tends to be simultaneously used for the observed effect itself, ie. for the ν-dependent displacement of components. To discern between the observed phenomenon and the geometrical interpretation, for the former one we will hereafter use the name *apparent RFM*. To avoid multiple adjectives, sometimes we will just write 'RFM' (in single quotation marks) in the same sense. Consequently, 'RFM' refers to the observed change of components' separation, whereas RFM to the geometrical model (spatial association of ν with r).

The ν-independent separation of 'conal' components in pulsar profiles, ie. the lack of apparent radius-to-frequency mapping ('RFM') may indeed be considered as a direct consequence of the stream-cut geometry: in the limit of an infinitely narrow stream, any radiation (of arbitrary frequency) can only be observed when the line of sight is in the plane of the stream. Narrow streams then provide excellent conditions for the lack of the apparent RFM. The profile of PSR J0437−4715, with its fixed location of components, bifurcations, and double notches has then been identified as a clear example of a profile in which the seemingly conal components are in fact not conal at all – they originate from the sightline passage through streams which, when viewed down the dipole axis, resemble a star-shaped pattern, or a pattern created by blades of an indoor ceiling fan.

Double notches require the obscuring streams or stream-shaped non-emitting regions within a radially- and laterally-extended emitter. Since the notches are also observed in normal pulsars (B1929+10, and B0950+08), DRD10 have concluded that streams must be ubiquitous among pulsars. Therefore, the need to extend the conal classification scheme to include the stream-shaped emitters, has been emphasized (see Fig. 18 in DRD10).

Precessing pulsars provide a direct way to map pulsar beams in 2D. However, conal beam models have not been able to reproduce the observed pulse evolution precisely (Kramer 1998; Clifton & Weisberg 2008; Lorimer et al. 2006; Burgay et al. 2005). This has lead to proposals of several beam shapes (hourglass, Weisberg & Taylor 2002; horseshoe, Perera et al. 2010) which nevertheless had overall morphology similar to the conal beam. DRD10 (Sect. 6.3.3 therein) suggested that the problems with the modelling of precessing beams are caused by the use of conal beams instead of the fan-shaped ones. A fan-shaped beam has explicitly been proposed for J1906+0746, based on the stability of its main pulse shape on a few-years-long timescale.

That prediction of a stream emitter in J1906+0746 has recently been confirmed by the beam map of Desvignes et al. (2013), although their geometrical solution is not well constrained (dipole tilt α with respect to the spin axis is equal to 81^{+1}_{-66} degrees). An azimuthally-limited emitter has also been deduced by Manchester et al. (2010).

The maps of precessing pulsars have recently been reproduced in Wang et al. (2014), who analyse statistical distributions of average profile properties in terms of both conal and fan models. Their distribution of pulse widths as a function of impact angle provides further credence for the ubiquity of the fan-shaped geometry of pulsar beams.

A major obstacle for the acceptance of the fan-beam geometry comes from the multiple-component profiles classified as T-, Q- and M-type by Rankin (1983; 1993). This is because they exhibit a wide range of phenomena that look deceptively conal. In particular, the peak-to-peak separation between their components increases with decreasing frequency, and this phenomenon is stronger for the outermost pair (eg. Mitra & Rankin 2002). For years this has been interpreted as the consequence of the fact that in dipolar magnetic field the outer circumpolar field lines are more strongly flaring away from the dipole axis than the inner ones.

The conal model was also applied to the lag of the central component with respect to centroids of 'conal' pairs, as observed in B0329+54 (Gangadhara & Gupta 2001, hereafter GG01) and other objects (Gupta & Gangadhara 2003, hereafter GG03). However, the lag had to be interpreted through a complicated structure of a near-surface emission region and several emission rings located at disparate altitudes. Altitude-dependent effects of aberration and retardation (AR), differentially deflecting the emission from the rings, were responsible for the observed delay. The AR effects with spatial RFM were also able to justify why the magnitude of the lag increases for decreasing frequency (GG01; Dyks et al. 2004).

The conal beam model was also supported by the statistical distributions of pulse width (and components' separation) versus rotation period (Rankin 1990; 1993; Gil et al. 1993; Kramer et al. 1994). All of them seem to suggest that widths of pulsar profile (and angular radii of cones) follow the inverse square root dependence on the rotation period P. This could imply that the fixed-intensity outer envelope of pulsar emission and dimensions of cones follow the flaring shape of polar tube. The derived dimensions of cones could even find a theoretical justification (Wright 2003). However, this does not exclude the possibility of the azimuthal structure of the beam. Moreover, the axisymmetric beam geometry is involved in some assumptions (eg. determination of α from the width of the central component) that have been used to obtain these results.

In this paper we apply the implications of the broadband emitting streams to normal radio pulsars, especially those of T, M and Q type, which can probably be considered as the prototype of conal thinking. We focus mostly on the frequency evolution of profiles, using the approach of DR12 (Fig. 2 therein), ie. by considering the geometry of fixed-intensity patterns in the vicinity of the line of sight. Several results of this paper apply also for the patchy beams of Lyne & Manchester (1988), since a single fan-shaped subbeam can be considered as a type of an elongated patch (Fig. 1). We will also consider circular patches of emission as a zeroth-order model for more realistic elongated beams. However, in the case of a fan beam emitted by a stream, the beam's elongation is explicitly identified: it is latitudinal and related to the curvature of B-field lines. In the case of a general patchy beam, the elongation or geometry of patches is less constrained. For example, if a patch is elongated mostly in

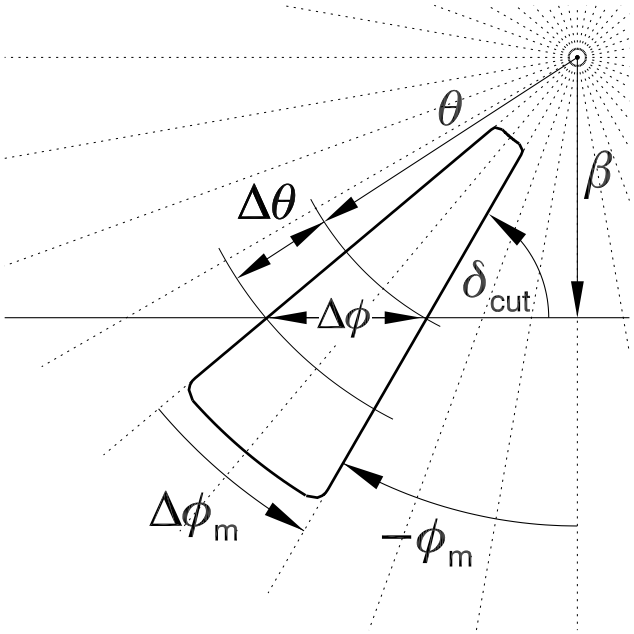

Figure 1. Sky-projected geometry of azimuthally-limited emission beam (thick contour) viewed down the dipole axis (top right dot). The horizontal line marks the path of the line of sight. Dotted lines present dipolar magnetic field lines. The azimuth ϕ_m is measured counterclockwise from the main meridional plane.

the magnetic azimuth, then the location of components in a profile is determined by the conal aspects of geometry. This is the case for the partial cones shown in Fig. 18 of DRD10 (middle sightline). In the present paper we focus on the latitudinally-extended patches (fan beams).

The paper is organized as follows. After a short introduction of key parameters of our model (Sect. 2) we show how the model leads to the apparent RFM effect (Sect. 3). In Sect. 4 we connect the apparent RFM with the spatial emissivity distribution in pulsar magnetosphere. The lag of a central component with respect to a midpoint between outer components is explained in Sect. 5, followed by Sect. 6 which discusses possible obscuration effects.

2 MAIN PARAMETERS OF THE STREAM MODEL

The dipolar magnetic field is assumed in this work. Because of the divergence of dipolar field lines, the radio-emitting region, when viewed down the dipole axis $\vec{\mu}$, typically has the form of a wedge. The region extends over a limited range of magnetic azimuth ϕ_m measured around the dipole axis, as well as over a limited range of magnetic colatitude θ_m, which is the angle between the radial position vector of an emission point and the dipole axis. In the dipolar field, radiation from a point at θ_m propagates at the angle $\theta \approx (3/2)\theta_m$ with respect to $\vec{\mu}$. Therefore, the associated beam (thick-line contour in Fig. 1) extends over a range of θ that can be directly translated into θ_m. The propagation angle θ is marked in Fig. 1. The beam extends azimuthally over $\Delta\phi_m$ – the same range of ϕ_m as the underlying stream. The latitudinal elongation of the wedge-shaped beam in Fig. 1 results from the 2D projection of the curved stream on the sky.

The observer's sightline probes the beam along the horizontal[1] line in Fig. 1 and it crosses the beam at the cut angle $\delta_{\rm cut}$ measured between some fixed magnetic azimuth ϕ_m within the beam and the sightline's path (both of them projected on the sky). The passage through the wedge beam lasts for a limited interval of pulse phase ϕ (pulse longitude). Fig. 1 shows that the passage through the beam (lasting over the interval $\Delta\phi$) corresponds to a change in angular distance from the dipole axis $\Delta\theta$. Assuming that streams follow the bent B-field lines, the passage must also be associated with a gradual change in detectable radial distance r from the centre of the star. It is important that the probed range of angular distances from the dipole axis ($\Delta\theta$) increases when the beam is cut at a smaller angle $\delta_{\rm cut}$. For orthogonal cuts ($\delta_{\rm cut} \sim 90^\circ$), as well as for extremely narrow streams, $\Delta\theta \sim 0$.

The cut angle is a crucial parameter in the stream model. As will be shown below, it is responsible for several aspects of the longitude-and-frequency-dependent behaviour established for multiple-component pulsars. In some cases the cut angle $\delta_{\rm cut}$ basically mimics the effect of flaring of polar tube. The cut angle is equal to $\delta_{\rm cut} = 90^\circ - \psi_{PA}$ (see eq. 6 in DR12), where ψ_{PA} is the polarisation position angle measured from the main meridional plane, containing the dipole and rotation axes. In the flat case with large $\alpha \sim 90^\circ$, we have $\delta_{\rm cut} = 90^\circ - |\phi_m|$ (Fig. 1).

We additionally use the standard geometrical pulsar parameters: the dipole inclination angle α with respect to the rotation axis $\vec{\Omega}$, the viewing angle ζ between $\vec{\Omega}$ and the observer's line of sight, and the impact angle $\beta = \zeta - \alpha$. We will also use the footprint parameter s, which is the transverse distance from the dipole axis, normalized by the transverse radius of the open field line region (both measured at the same radial distance r).

3 ORIGIN OF THE OBSERVED RADIUS--TO-FREQUENCY MAPPING

By the 'observed RFM' (or apparent RFM, or just 'RFM' in single quotation marks) we mean the change of peak-to-peak separations between components observed at different frequencies, and the associated change of pulse profile width.

To illustrate its origin within the stream model we will temporarily assume that the sky-projected pattern of radio emission at a fixed frequency has a circular shape with the radio intensity decreasing away from the centre (Fig. 2). One can imagine a two dimensional (axially-symmetrical) Gaussian projected on the sky. Emission at a fixed ν is not constrained to the interior of a circle only. It may be thought that the circles present, say the 50% intensity level, with the peak emissivity at the centre of each circle. Assuming that the spatial RFM exists and magnetic field lines flare away from the dipole axis, the low-frequency patterns should be located further away from the axis. This is shown

[1] For simplicty we ignore all spherical trigonometry issues that are not important for the illustration of our arguments.

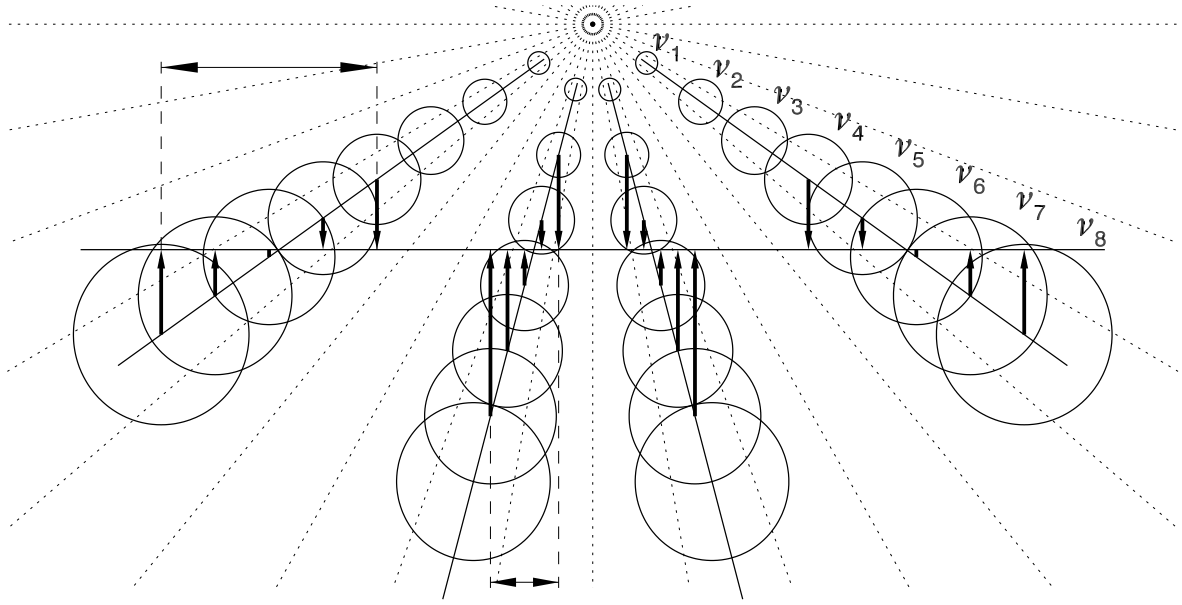

Figure 2. The mechanism of the apparent radius-to-frequency mapping. Circles of different size represent fixed-intensity contours at different frequencies, with the maximum intensity at the their centres. Longitudes of observed peak flux at different ν are marked with vertical arrows. The equidistant locations of the consecutive ν-contours (same for all beams) represent the same angular spectral gradient along all four beams. Note the smaller frequency-dependent spread of the inner components (bottom horizontal arrow) compared to the outer components (top horizontal arrow).

with the sets of solid circles in Fig. 2. The circles that correspond to lower frequencies become larger because the emitting stream/wedge becomes wider at larger distance from the dipole axis.[2] Since the intensity at a fixed frequency is monotonously decreasing with the distance from the centre of each circular contour, a component's peak will be observed when the line of sight is closest to the centre of a circle corresponding to a given frequency. These phases are marked with vertical arrows, which show clear change of peak location with frequency.

An equivalent description is to say that the emitted spectrum changes along the stream, and, during the passage through the stream, the line of sight samples different spectra. However, if the angular variations of a locally-emitted spectrum are ignored, the interpretive capabilities of the model are seriously hampered. Therefore, we introduce the 'angular spectral gradient' which provides a measure of how strongly the spectrum changes with angular separation on the sky. For example, the θ-component of the gradient can be defined as $d\langle\nu\rangle/d\theta$, where $\langle\nu(\phi_m,\theta)\rangle$ is the average frequency emitted in direction (ϕ_m,θ), weighed by the spectral distribution of intensity. Unless otherwise specified, the term 'angular spectral gradient' will hereafter refer to the change of spectrum with θ (at a fixed ϕ_m). It will also be called the 'θ spectral gradient'.[3] Below we will also use other types of spectral gradients, eg. the radial (spatial) one. We will also refer to the angular scale of spectral change in direction θ. This θ spectral scale is proportional to $d\theta_{\rm pk}/d\nu$, where $\theta_{\rm pk}(\nu)$ is the colatitude of the centre of a pattern at the frequency ν. In Fig. 2, this scale is visualised as the separation of the circular contours corresponding to different frequencies. It is worth to emphasize that the same-size contours on different streams in Fig. 2 do not necessarily need to represent the same ν. Their size increases just to represent the widening of the emission region with θ.

When the line of sight cuts through a few streams with similar angular spectral gradient, the inner components exhibit weaker 'RFM' (Fig. 2). This is because the beams of inner streams are cut more orthogonally, and a given angular displacement of the fixed-ν patterns, translates to a smaller shift in pulse longitude. This is marked in Fig. 2 with two horizontal arrows. Note that the θ-separations of the fixed-ν patterns are the same for all streams in Fig. 2 just to illustrate how a given angular spectral gradient transfers onto the strength of the observed 'RFM'. In real pulsars the angular spectral gradient may depend on θ and may be different for streams with different s. However, it may also be different for streams which differ in ϕ_m only, because the acceleration strength can vary with the distance from the main meridian (MM), which contains both the rotation axis and dipole axis (eg. Arons & Scharlemann 1979). As we discuss in Sect. 4 the spatial RFM illustrated by the circles in Fig. 2 is likely caused by both the radial and transverse drop of density in the emitting streams.

An immediate consequence of the stream geometry is the expectation of weak (or nonexistent) 'RFM' in three cases: 1) When the spectral properties of the locally-emitted radiation do not change within the observable part of the stream. For example, all points within the beam may emit a spectrum with the same shape but different normalisa-

[2] The diameter of the low-ν patterns can also be additionally enlarged by the increasing size of microphysical beams (elementary beams of the emitted radiation, see DR12).

[3] The ν-dependent intensity can change also in ϕ_m direction (Fig. 3) so the gradient is two-dimensional. For brevity, however, we will use the name 'gradient' instead of the 'θ-component of the gradient'.

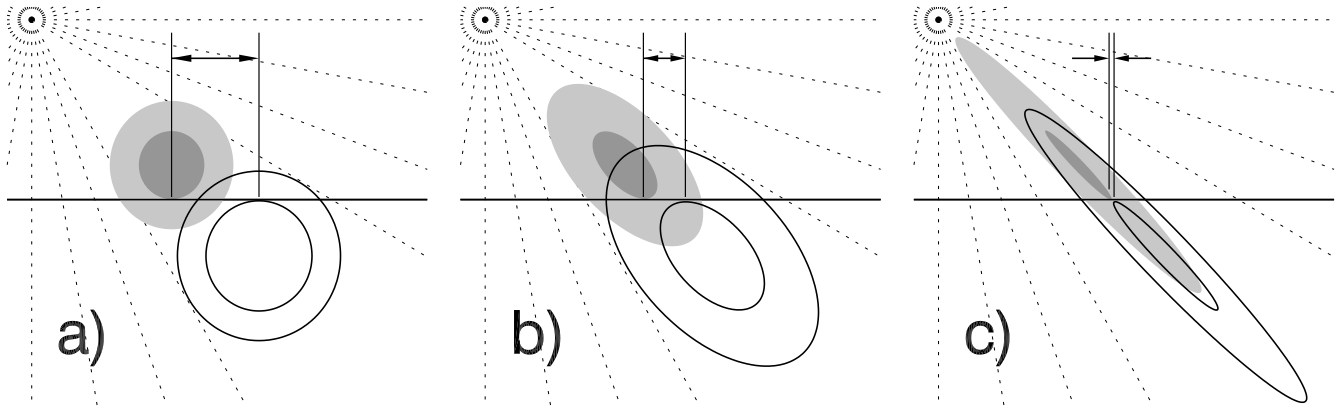

Figure 3. Sky-projected emission from three streams with the same ϕ_m but different angular spectral structure. Fixed-intensity contours at two frequencies (ν_1 and ν_2) are shown for each beam, with two levels of intensity marked for each ν. One frequency is marked with the grey contours, the second – with the solid line contours. The beams become more broadband from left to right, as marked by the increasingly overlapping contours of different ν. The levels of larger intensity (inner contours) were selected to expose the location of peak flux of observed pulse components, ie. they are tangent to the path of the line of sight (the solid horizontal). The marked phase intervals present the dislocations of components which correspond to the fixed frequency interval $\nu_1 - \nu_2$. **a)** The circular fixed-ν contours, which are useful to expose the role of $\delta_{\rm cut}$. **b)** More realistic, θ-extended contours for a moderately narrow-band emission. **c)** A broad-band beam expected for MSPs and pulsars with no apparent RFM. In c), the apparent RFM is additionally decreased by the narrowness of the beam.

tion. A case with weak spectral changes in the θ direction is shown in Fig. 5. 2) When the streams/beams are extremely narrow and emit the fixed-intensity patterns in the form of narrow ellipses such as shown in Fig. 3c and 5. Then the arbitrarily-large angular separations of the fixed-ν contours cannot much change the position of a component. If the spread of contours in θ is very large, the component will just disappear. 3) When a single-component profile is produced by a meridional stream ($\delta_{\rm cut} \sim 90^\circ$); in this case the component's peak position is ν-independent, although the component's width may vary with frequency.

We conclude that the merging of components with increasing frequency observed in T, Q and M pulsars, as well as the frequency evolution of their width, can be naturally interpreted within the fan beam model. The smaller rate of 'RFM' observed for the inner pair of components in Q and M pulsars, results from the larger cut angle $\delta_{\rm cut}$. It is not related to the weaker flaring of the hypothetical emission region located at the inner polar magnetic flux tube.

The multistream symmetry of Fig. 2 is consistent with the ubiquitous (though approximate) left-right symmetry of profiles: the outer components are (on average) cut at a larger θ from the dipole axis. If all streams are spatially equidistant from the dipole axis (ie. have the same footprint parameter s) then the inner components are viewed at smaller r. They can therefore differ from the outermost components, having different flux, spectrum, or shape. The same argument refers to the central component ('core'), which is a stream viewed closest to the dipole axis. The stream model then retains the capability of conal model in reproducing the roughly mirror-symmetric properties of profiles.

Note, that the mechanism of the ν-dependent displacement of components, illustrated in Fig. 2, works whenever a spectrally non-uniform beam is cut at $\delta_{\rm cut} \neq 90^\circ$, regardless of whether the spatial RFM exists or not. However, the width of the majority of profiles increases with ν (Hankins & Rankin 2010), which seems natural for the upward decrease of plasma density. The spatial RFM also provides a way for symmetry breaking by the AR, as described in Sec. 5.2. Therefore, it is reasonable to relate the θ spectral gradient with the changes of the emitted spectrum along the stream, ie. with different emission altitudes.

The stream model is then capable to produce the apparent RFM effect. A hint of this capability is visible in Figs. 2 and 3 of DR12, where the peak of a bifurcated component jumps to a later pulse phase with increasing frequency. In the case of a single-peaked (non-bifurcated) component, its skewness would change and its peak would move rightward. The apparent RFM can be especially strong when streams are not too thin and when they are cut at small $\delta_{\rm cut}$.

The choice of observed frequency $\nu = \nu_0$ picks up specific contours in Fig 2. These ν_0-circles in different streams can be located above or below the horizontal sightline path in Fig. 2. If they are located above the path in the outermost streams, then the peak flux of outermost components will increase with decreasing ν. If at the same time the corresponding ν_0-contours in the inner streams (including a possible 'core stream'), are located below the sightline path, a decrease of observed ν will make the peak flux of the inner components smaller. Therefore, a change of observation frequency may reveal different spectral evolution of the inner pairs (or core) than that of the outer pair (eg. a brightening of the inner components at a simultaneous fading of the outer pair).

Obviously, for a detectable RFM to appear, the streams have to be spectrally-nonuniform. In general, different streams may have different θ spectral gradient. In Fig. 3 this effect is illustrated in the form of more overlapping and more elongated fixed-ν contours. This would result in different rate of component dislocation (and fading) with frequency, even when they have the same $\delta_{\rm cut}$ (as is the case in Fig. 3). Therefore, to obtain a more complete view of pulsar emission, it is necessary to allow for the convolution of the spectral gradient with the effects of $\delta_{\rm cut}$. Differences in the

spectral gradient likely exist in pulsars and contribute to the large variety of the observed behaviour of profiles (Hankins & Rankin 2010; Kramer et al. 1998).

One can imagine a model, in which the spectral gradient changes monotonously with the azimuthal distance ϕ_m from the MM. When convolved with the effect of $\delta_{\rm cut}$ shown in Fig. 2, this could change the rate of, stop, or reverse the apparent RFM. While such azimuthal spectral non-uniformity is possible, it does not automatically implies that the outer pair of components should exhibit stronger apparent RFM. The value of $\delta_{\rm cut}$ then remains the primary and unavoidable factor, which determines the relative rate of components' displacement. However, if the spectral differences between the beams are strong, they need to be superposed on the effect of $\delta_{\rm cut}$.

3.1 Weakness of the apparent radius-to-frequency mapping in millisecond pulsars

The key difference between the millisecond pulsars (MSPs) and normal pulsars is that B-field lines flare (bend away from the dipole axis) more strongly in the former case. For a fixed scale of radial spectral gradient, assumed to be universal for both the MSPs and normal pulsars, the traditional conal model would imply much stronger 'RFM' for the MSPs. However, if the radio frequency corresponds to the plasma frequency, emission at two frequencies should occur at radial distances which are at a fixed ratio, as determined by the frequencies. In that case an apparent RFM of comparable magnitude would be expected for both the MSPs and normal pulsars. In the bottom half of Fig. 4, conal emission regions for both types of pulsars have been illustrated for two frequencies at the same ratio of r. Available observational data (eg. Kramer et al. 1999; You et al. 2007) clearly contradict this expectation and show that MSPs do not exhibit the apparent RFM.

However, the lack (or weakness) of the 'RFM' in MSPs is naturally expected in the stream model. With more bent B-field lines, the streams in magnetospheres of MSPs are likely to produce beams that are more elongated in the θ-direction, and are more likely to be cross-cut by the line of sight. More importantly, however, changes of the spectrum with altitude are spread over a very elongated beam. Therefore, the spectrum emitted at different points in the vicinity of the line of sight, does not change much with θ. This corresponds to the overlapping and elongated fixed-ν patterns shown in Fig. 3c. In the case of normal pulsars, the radiation from within a much larger range of altitudes, ie. with a larger spectral diversity, is projected onto a much smaller angular area on the sky (see the top part of Fig. 4). Therefore, the spectrum changes on a smaller angular scale in the beam of normal pulsars. This corresponds to the less overlapping fixed-ν contours such as those in Fig. 3b.

In the case of the MSPs, radiation emitted in a specific direction has a larger spectral extent (is more broadband) than in the normal pulsars. While a stream of a MSP is being cut by the line of sight, the observer detects radiation from only a small portion of the stream's extent, because the radiation is emitted within a small angle $1/\gamma$ around the velocity vector (γ is the Lorentz factor) and the curvature radius ρ of the B-field lines is small. In the case of normal pulsars, with small curvature of B-field lines, at any instant

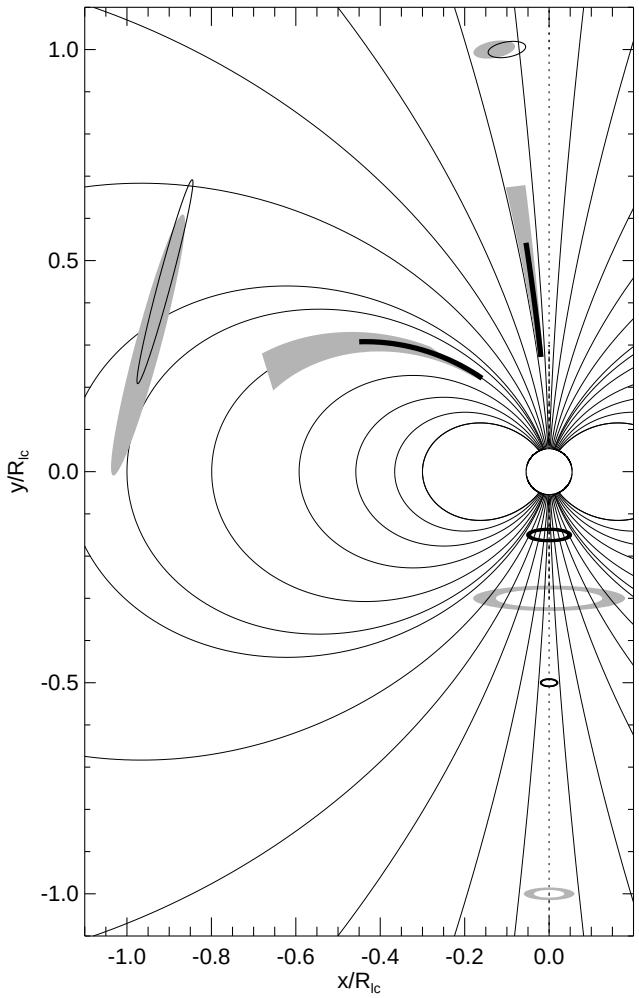

Figure 4. Approximate geometry of emission regions at two different frequencies. Bottom half of the plot presents the conal model whereas the top half – the stream model. Lower ν is marked in grey, higher ν – in black. Only the strongest-emissivity regions are marked for the conal model. Note the strong apparent RFM implied by the conal model for MSPs. For the stream model, the sky-projected beams are schematically presented on the far left (MSPs) and top (normal pulsars). See Figs. 3c and 3b, respectively, for a more clear presentation of the beams.

the observer probes a larger range of r. However, this larger Δr corresponds to a smaller range of plasma density, which can be shown as follows. In a dipolar field, the range of plasma density κ_{pl} is related to Δr through $\Delta\kappa_{pl} \propto r^{-4}\Delta r$, where $\Delta r \propto \rho/\gamma$, as implied by the size of the microbeam. For the curvature radiation with the peak frequency $\nu \propto \gamma^3/\rho$, the microbeam size is $1/\gamma \propto \rho^{-1/3}$. In a dipolar field $\rho \propto (rR_{lc})^{1/2} \propto (rP)^{1/2}$, so $\Delta\kappa_{pl} \propto r^{-11/3}P^{1/3}$. In MSPs r is two orders of magnitude larger, and P – two orders of magnitude smaller, than in normal pulsars. The range of plasma densities implied by the microbeam-size limitation is then much larger in the case of MSPs than in normal pulsars. The spectrum emitted in some direction (ϕ_m, θ) is, therefore, wider in the case of MSPs.

Another constraint on the range of plasma densities probed at a fixed (ϕ_m, θ) is related to the instantaneous visibility of the emission region in the case when the extent

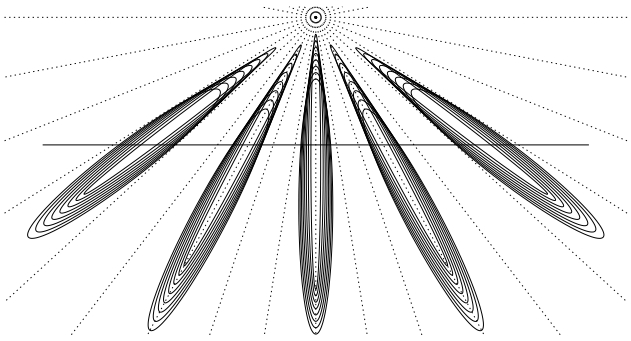

Figure 5. Example of a millisecond pulsar beam. The fan beams are longer and spectrally more uniform. Spectral changes in θ direction are nearly washed-out as marked with the overlapping fixed-intensity contours for different ν. The horizontal marks the passage of line of sight. In this case pulse components do not spread with frequency. The AR effects, which bend the beams leftward (see Fig. 11b), are neglected in this figure.

of the $1/\gamma$ microbeam is negligible (emission strictly tangent to B-field lines). For simplicity, let us ignore the aberration-retardation effects (described in Sect. 5), the issue of obscuration (Sect. 6) and the possible torsion of electron trajectories (hence of the stream shape). Then at a single pulse phase the line of sight can receive radiation from within a single plane of fixed ϕ_m within the emiter. The observer is simultaneously detecting radiation from all the points within the plane, where the B-field is inclined at a single angle θ with respect to μ. As shown in Fig. 6, in the dipolar field these points are located along a straight radial line with a fixed magnetic colatitude $\theta_m \approx (2/3)\theta$. Thick parts of the line, which overlap with the grey emission regions, are quasi-simultaneously visible by the observer. Fig. 6 shows two emission regions: the bottom one for a fast millisecond pulsar ($P \approx 5$ ms), and the upper one for a bit slower rotator. It can be seen that for a similar thickness of the streams in θ_m direction, the observer samples a smaller interval of r in the case of the MSP (bottom grey region). The above-discussed extent of the $1/\gamma$ microbeam affects this picture by providing some non-zero θ_m-width to the simultaneously detectable region. Despite the smaller $\Delta r(\phi_m, \theta)$, a similar estimate as for the microbeam size again implies more broadband emission in the case of MSPs.

For all these reasons (different length of detectable B-field line; different angular extent of projected emission, and different radial extent of detectable emission), the beams of MSPs are more elongated and more broadband than those of normal pulsars. Cutting through the beams of millisecond pulsars then resembles the situation presented in Fig. 5, with more elongated beams, and the spectrum weakly evolving along the beam. The wider frequency extent of the spatially more-localised spectrum is consistent with the simpler shapes of MSPs' spectra, as described in Kramer et al. (1999), cf. the spectra of normal pulsars in Malofeev et al. (1994), Kuzmin & Losovsky (2001), and Maron et al. (2000).

4 MAPPING THE APPARENT RFM BACK INTO THE PULSAR MAGNETOSPHERE

The problem of mapping the observed flux back into the dipolar magnetosphere is a complex issue. The necessary mathematical formulae can be found eg. in DRD10. In general, however, even with a complete information on the viewing geometry and location of the stream, it would be difficult to recover the ν-dependent 3D magnetospheric emissivity distribution from a pulse profile. A useful partial insight can nevertheless be gathered from consideration of possible meridional distributions of emissivity.

When the line of sight is crossing the stream, it moves both in the magnetic azimuth ϕ_m and colatitude θ (Fig. 1). The properties of polar zone (such as the acceleration potential) are expected to depend on magnetic azimuth ϕ_m and individual streams may be asymmetric in ϕ_m. However, a localised plasma stream, ie. a narrow stream with large transverse gradient of plasma density, can possibly be considered roughly symmetric with respect to its own central plane, ie. symmetric on both sides of the mid-stream azimuth $\phi_m = \phi_{m,0}$. Under this assumption, the plane of the fixed $\phi_{m,0}$ (containing the centre of the stream and the dipole axis) becomes most usefull to apply the inverse engineering to 'RFM'. We will thus focus on the latitudinal motion of the sightline in θ-direction because emission properties are expected to change monotonically with r and θ (or θ_m). With the approximate ϕ_m-symmetry assumed, the transverse motion of the line of sight in the ϕ_m direction will just convolve a roughly symmetrical bell-shaped flux profile with the asymmetric flux changes resulting from the motion in θ.[4]

Fig. 7 presents an emission region (stream) with a plasma density gradient in the $\phi_{m,0}$-plane. Darker contours mark denser inner parts of the stream. The contours of fixed density have been calculated for a Gaussian lateral distribution and take into account the 3D spatial divergence of B-field lines. Thus, the usual dipolar decline of density with r is included, though more sophisticated complications (such as the null-charge surface) are neglected. It is assumed that the iso-density contours also present the contours of fixed emissivity at a corresponding frequency, with a lower frequency being emitted from a lower density region. Finally, since we discuss averaged (or integrated) pulse profiles, the density distribution represents a long-timescale average of instantaneous density in pulsar magnetosphere.

Thick straight lines in Fig. 7 present five simultaneous-visibility regions corresponding to five different pulse longitudes in the profiles shown in the inset. We assume that the stream extends at some angle $\phi_{m,0} < 0^\circ$ towards the leading side (LS) of the magnetosphere ie. towards the direction of rotation (Fig.1). The azimuthal extent of the stream ($\Delta\phi_m$) is assumed to correspond to the pulse longitude interval 1-5. In the absence of any radial (longitudinal) decline of emissivity, the azimuthal emissivity profile which is perfectly symmetric with respect to $\phi_{m,0}$, would produce the al-

[4] Azimuthal density distribution may be more important for nearly meridional or very narrow streams, however, since they are expected to exhibit little 'RFM', we will discuss the latitudinal density pattern. Some aspects of the lateral profile in the ϕ_m-direction are shown in Fig. 3. See also Sect. 6.

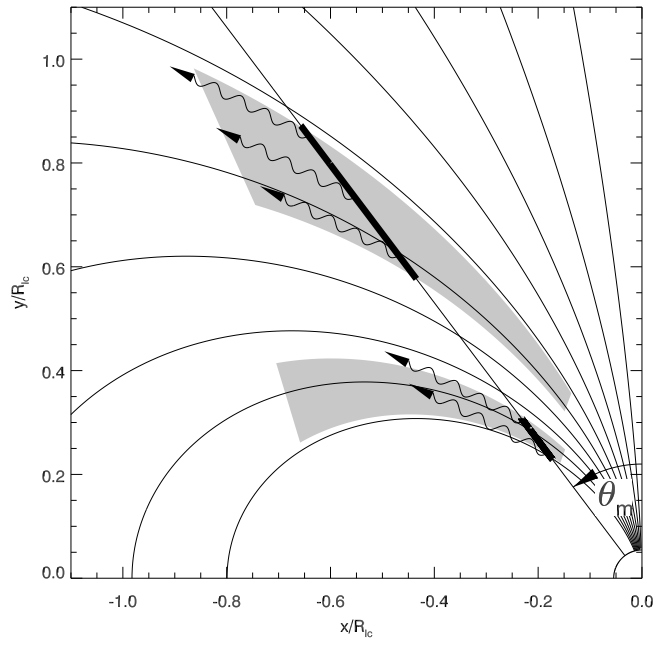

Figure 6. Geometry of a region (tilted radial line) from which radiation is detectable almost simultaneously. With emission constrained to the grey contours, the region becomes limited to the thick sections of the radial visibility line. In the absence of AR effects, all the wavy rays should be observed at the same pulse longitude.

most symmetric bell-shaped pulse component shown above the inset.[5] To estimate the ν-dependent behaviour of the component in the case of the radially-nonuniform emissivity, the radial emissivity profile needs to be convolved with the azimuthal bell.

In general, our line of sight can enter the stream at *any* angular distance from the dipole axis, because this depends on both the stream location and viewing geometry. In the case shown in the inset, this happens at such an angle θ that corresponds to θ_m marked by the radial visibility line no. 1. During the passage through the stream the sightline approches the dipole axis and receives radiation from radial visibility lines with smaller θ_m, ie. located closer to $\vec{\mu}$. Near the pulse phase marked with the number '2' (see the inset), a maximum of the lowest-ν component is observed, because the radial visibility line is detecting radiation from the bulk of the corresponding low-density region (the light-grey lobe that extends to $x/R_{lc} \approx -1.07$). Note that only that part of the emission region which overlaps with the line no. 2, is detectable at the pulse longitude which is marked with number '2' in the inset. When the line of sight is moving further through the pulse component (to longitudes 3, 4, and 5), the visibility line is progressing to locations 3, 4, and 5. This increases the contribution of the high-ν radiation, and diminishes the low-ν flux, as shown in the inset.

[5] This azimuthally-shaped component would not be perfectly symmetric, because the speed at which our line of sight probes consecutive ϕ_m changes with pulse longitude, as demonstrated by the S-swing of the polarisation position angle. We ignore this effect to expose the role of the radial emissivity profile.

The line of sight can exit the beam at any θ_m depending on the azimuthal width $\Delta\phi_m$ of the stream and the observers' viewing angle. In the case illustrated in the inset of Fig. 7, the sightline probes quite a large range of θ_m before exiting the stream. This happens when the beam is wide (large $\Delta\phi_m$) or when it extends at a large azimuthal angle with respect to the meridional plane ($\phi_m \sim 90^\circ$, $\zeta \approx \alpha$). Note that the flux decline in the wings of the discussed component is caused by the azimuthal motion of the sightline. Even though Fig. 7 presents only the latitudinal motion, the effects of the azimuthal motion on the shape of components are included in the inset of Fig. 7.

Since the stream we have considered was positioned on the LS, our line of sight was *approaching* the dipole axis during the passage through the stream. To obtain the illusion of a cone, another component, located symmetrically on the trailing side (TS) of the profile would have to be produced by another stream, located roughly symmetrically on the TS of the MM. Should such a stream exist, our sightline would sample the visibility sections in a reversed order (5 to 1), and produce the trailing component shown in the inset.

Depending on the geometry involved, at the moment when our line of sight is entering the stream, the corresponding radial visibility line can have any angle with respect to the dipole axis. The range of θ_m probed in Fig. 7 depends on the central azimuth of the stream $\phi_{m,0}$, the width of the stream $\Delta\phi_m$, and the observer's impact angle β. For example, let us consider a more meridional (or just narrower) stream with identical density distribution as before. The line of sight can enter the emission region at the visibility line 3, and quickly exit the beam at the line no. 4. In such a case, the low-ν radiation would still be observed, but the low-ν pulse component would become weaker, in comparison to the same-frequency components described before (as well as in comparison to the components at higher ν). This is because the peak flux of the observed low-ν component must now be located roughly mid-way between pulse longitudes '3' and '4', as determined by the new azimuthal emissivity profile (not shown in Fig. 7). At this phase, however, the low-ν emissivity is weaker (see the top profile in the inset of Fig. 7). Therefore, the observed spectrum of a given component is selected by the path of the line of sight within the stream (in addition to being determined by intrinsic factors such as the emission physics). In the presented case, ie. for emission altitude quickly increasing with decreasing ν, the outer components should have softer spectra than the inner components, ie. the outer components should increasingly dominate in the profile at lower frequency. This phenomenon is observed in several pulsars, eg. in the case of B1237+25 (Hankins & Rankin 2010).

A more general case is shown in Fig. 8, in which the transverse arrangement of emission regions that correspond to different frequencies (and densities) is shown as before with the grey-scale contours. However, it is now assumed that the local emissivity within each fixed-ν region changes with altitude. Five possible radial (more precisely – longitudinal) profiles of emissivity are considered within the stream. In each case the local emissivity increases along the stream until reaching a maximum at some r, then falls off with further increase of the distance along the stream. For each case, the maximum of emissivity within the stream is marked with sections of straight lines: dashed, dot-dashed, and dotted

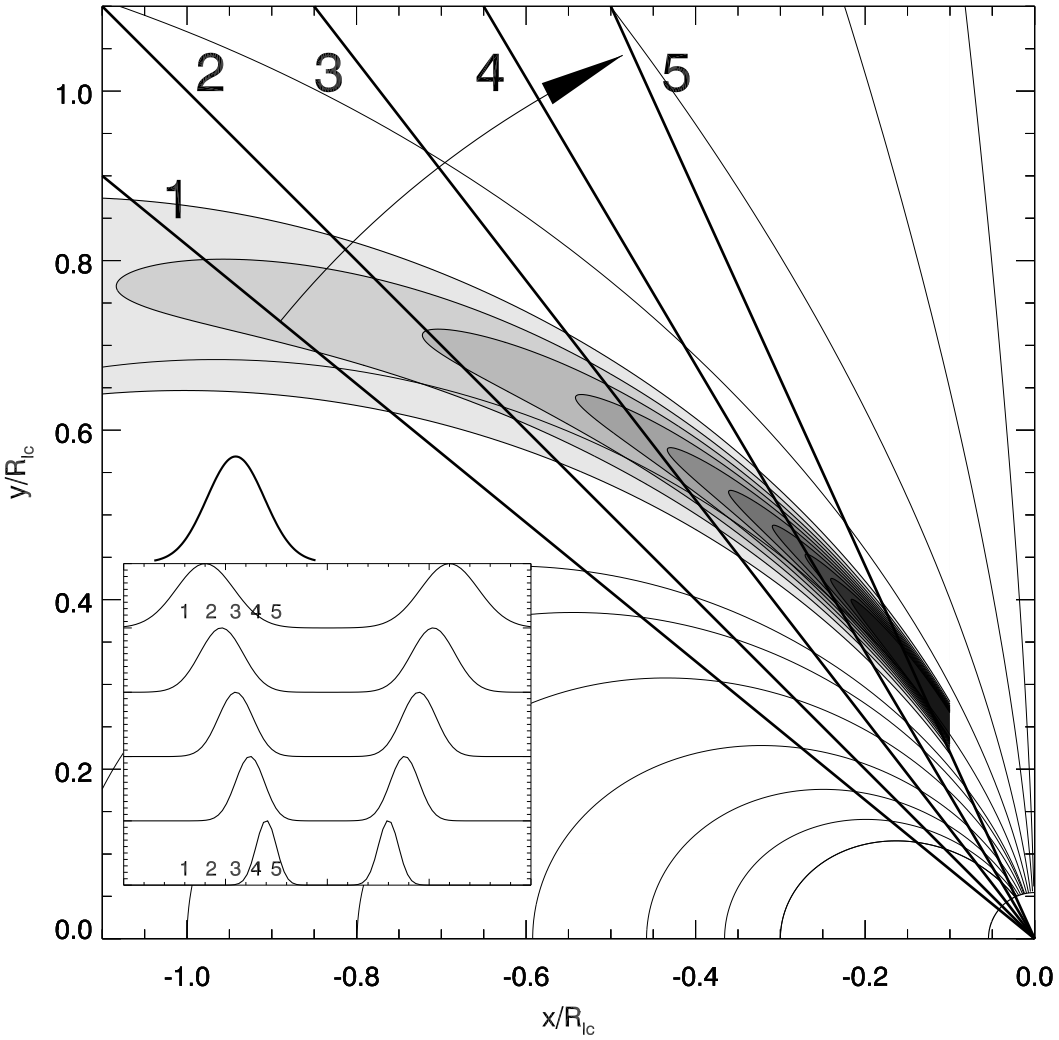

Figure 7. Contours of equal density in the plane of the stream's central azimuth $\phi_{m,0}$. When the line of sight is passing through a leading-side stream, it is probing increasingly deeper regions marked with the visibility lines 1-5, which correspond to pulse longitudes marked in the inset. Therefore, the high-frequency emission dominates at later longitudes within the 1-5 pulse phase interval. The frequency increases from top to bottom in the inset. The bell-shaped curve above the inset presents the azimuthal emissivity distribution within the stream, which needs to be convolved with the radial profile shown with the grey contours, to estimate the locations of the components in the inset. See text for more details.

(three cases). We will discuss them in the clockwise order, starting from the dashed case. Pulse profiles that correspond to different cases are presented in the three insets in the bottom left corner. In each of them the low-frequency profile is on top.

The sightline is assumed to enter the stream from a side at pulse phase '1', corresponding to the visibility line no. '1'. Then the sightline moves obliquely through the stream and exits it at phase '2', associated with the visibility line no. '2'. The low-density region that overlaps with a visibility line is split in two parts, one on the top, another on the bottom side of the stream. The question on whether the radiation from the bottom part can reach the observer is difficult and depends on several factors, such as the polarisation of the emitted wave, and the temporal/spatial variations of plasma density in the stream. A qualitative inclusion of the bottom-side emission would require an interesting, but lengthy analysis of a more complicated version of Fig. 8. For brevity, therefore, it is now assumed that the bottom side of the stream (the part of the stream on its concave side) contributes little to the observed flux.

The dashed line presents the case when the altitude of peak emissivity steeply decreases with increasing frequency. A cut through a stream with such a property would result in normal 'RFM', shown in the bottom inset of Fig. 8. This is because the strongest low-ν emission is observed early in the 1-2 phase interval, when the observer is sampling visibility lines located close to the line no. '1'. High-ν emission will peak closer to phase '2', since the high-ν emissivity is strongest nearby the visibility line no. '2'. We remind that the decline of flux at the edges of the 1-2 interval is caused by the azimuthal emissivity profile, which needs to be convolved with the radial profile peaking at the dashed line.

The dot-dashed line presents the fixed-θ_m case when

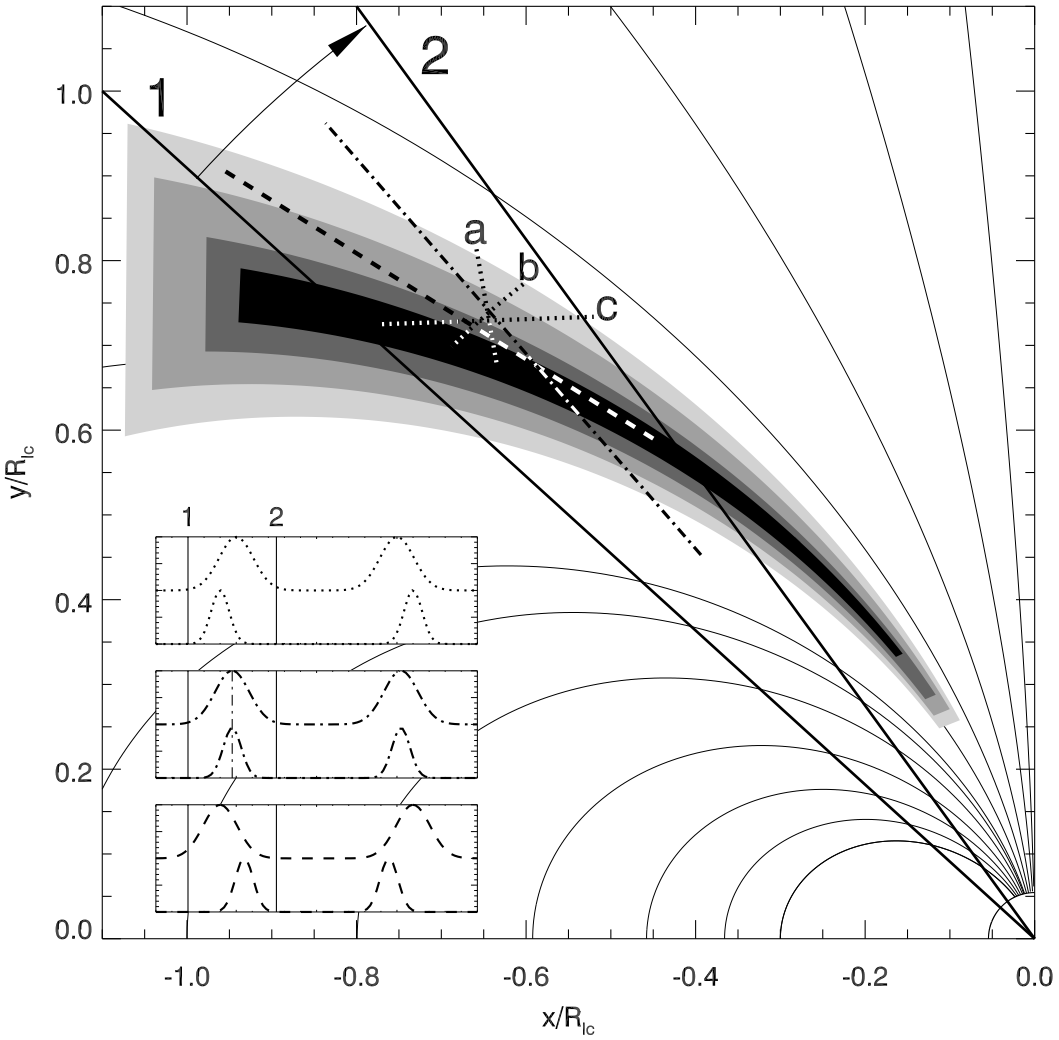

Figure 8. The influence of spatial emissivity distribution on the ν-dependent displacement of components. Grey contours of different grade show emission regions for different frequencies. Locations of peak emissivity are marked with the dashed, dot-dashed, and dotted sections of straight lines. The corresponding pulse profiles at two frequencies (with lower ν always shown on top) are presented in three insets. The dot-dashed line separates the cases of normal 'RFM' from anti-'RFM' behaviour. See text for more details.

all frequencies peak roughly in the middle of the 1-2 phase interval. This would not induce much 'RFM', because the convolution of two coincident bell-shaped profiles does not change the peak's position (see the dot-dashed components in the middle panel of the inset). Thus the dot-dashed section is a separatrix between the normal 'RFM' and the inverse 'RFM', in which case the lower-ν profiles would be observed closer to the centre of the profile.[6] The speed at which the line of sight crosses consecutive azimuths ϕ_m increases towards the MM, as has always been illustrated by the S-swing of the polarisation position angle. Therefore, the separatrix that corresponds precisely to the centre of the 1-2 pulse interval is located not exactly in the middle between the visibility lines '1' and '2'. For the leading component shown in Fig. 8, the separatrix is closer to the visibility line '2'.

An interesting case leading to the inverse apparent RFM is represented by the first dotted line, marked 'a'. The spatial RFM is normal in this case, with the peak emissivity located at a larger r for the lower-ν region. However, the low-ν radiation peaks at a later phase (closer to the visibility line '2') than the high-ν emission, that peaks closer to phase '1'. This is then the case when the normal spatial RFM leads to the inverse apparent RFM, illustrated with the dotted profiles in the top inset.

The second dotted line, marked 'b', presents the case with no spatial RFM. The peak emissivity at all frequencies occurs at the same radial distance r. The line 'b' is then orthogonal to the separatrix described above. Orientation of the dotted line with respect to the visibility lines '1' and '2' reveals that the low-frequency component (top curve in

[6] The lack of 'RFM' is a frequently observed feature of several pulsars (eg. Gould and Lyne 1998). It can be interpreted through the coincidence of the peak-emissivity separatrix with the centre of an observed component. Another explanation involves a quasi-uniform longitudinal emissivity distribution within the entire region between the visibility lines '1' and '2'.

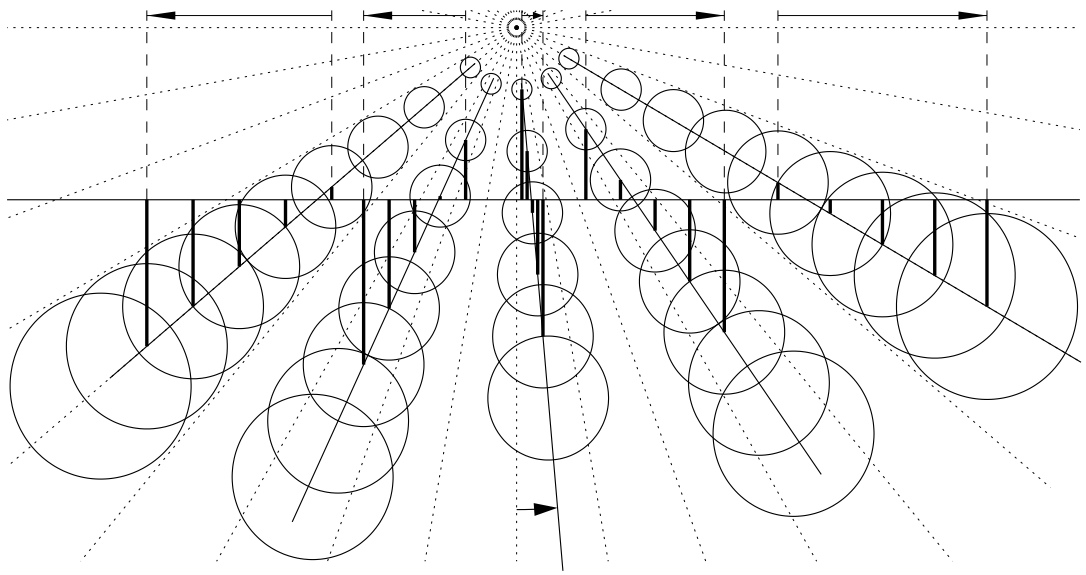

Figure 9. The mechanism of the accidental lag of the central component with respect to the centroids of pairs of outer components. The beam structure is symmetric with respect to the central beam, but it is rotated by the angle ϵ (bottom arrow) with respect to the MM. All the beams have the same θ spectral gradient. The arrows on top show the components' displacements for decreasing ν. The model produces a lag of the central component which is increasing with decreasing ν (see text).

the top inset) will definitely peak closer to phase '2', whereas the high-ν component closer to phase '1'. This is the case when the lack of spatial RFM results in the inverse apparent RFM.

The nearly horizontal dotted line 'c' presents the case with the altitude of peak emissivity steeply decreasing with decreasing ν. It produces a similar profile evolution as in the previous case (top inset).

Thus, the frequency-dependent behaviour of profiles ('RFM', no 'RFM', or inverse 'RFM'), depends on the spatial emissivity distribution around the fixed-θ_m separatrix that corresponds to the central azimuth of the stream $\phi_{m,0}$. Since the majority of pulsars exhibits normal RFM, it is concluded that typically the altitude of the strongest emissivity at a given frequency quickly increases with decreasing ν, as the straight dashed line shows qualitatively. This is consistent with the common expectation of plasma density drop with altitude illustrated by the contours in Fig. 7. Interestingly, however, it is possible to observe the reverse RFM even for the peak-emissivity altitude increasing with decreasing ν (case 'a').

5 ORIGIN OF THE FREQUENCY--DEPENDENT LAG OF THE CENTRAL COMPONENT

Position of a central component in multiple-component profiles often lags a centroid located half way between outer components. GG01 have shown that this can be caused by the aberration and retardation (AR) effects operating at different emission altitudes of the core, inner cone, and outer cone. The AR-induced shift of a centroid is approximately equal to $\Delta\phi \approx 2\Delta r/R_{lc}$, ie. it depends only on differences in emission altitude (Dyks et al. 2004). It has therefore been widely used to determine r as well as the transverse distance of the cones from the dipole axis, ie. the footprint parameter s (GG01; GG03). However, the ensuing structure of the radio emission region (with a variety of r and s) have revealed unacceptable arbitrariness, difficult to interpret in terms of physics. For example, instead of the lateral separation of emission rings (Ruderman & Sutherland 1975; Wright 2003), for PSR B0329+54 GG01 invoke as many as four radially-separated emission cones at roughly the same B-field lines ($s \sim 0.6$). As found in GG03 (and adjusted in Table 1 of Dyks et al. 2004), the set of the hypothetical emission rings can be located near the dipole axis ($s \in (0.3, 0.4)$, PSR B2111+46), distributed around a moderate distance from the pole ($s \in (0.3, 0.6)$, B1237+25) or placed close to the polar cap rim ($s \in (0.7, 0.9)$, B1857−26).

As soon as one allows for the azimuthal structure of the radio emission region, the centroid shift can be understood without invoking emitters at disparate altitudes. As we show below, with several streams extending within the same altitude range, the shift can still be understood in two ways: 1) through the altitude-dependent AR effects that break the symmetry of the system of streams (Sect. 5.2), and 2) just through an accidental asymmetry of location of the beam system with respect to the MM, whatever is the reason for the asymmetry. In the latter case, discussed in the next subsection, the centroids are shifted regardless of emission altitudes, ie. the shift is non-zero even for exactly the same emission altitude within the entire emission beam ($r = r_0$, $\Delta r = 0$). The AR effects are not involved in this mechanism. The key factor that leads to the centroid shift in both mechanisms, is the asymmetry of streams/beams with respect to the MM, with the cut angle $\delta_{\rm cut}$ again responsible for the frequency-dependence of the phenomenon.

Below we test the two mechanisms against the observed properties of the centroid shift phenomenon. We start with the simple case with no AR effects included.

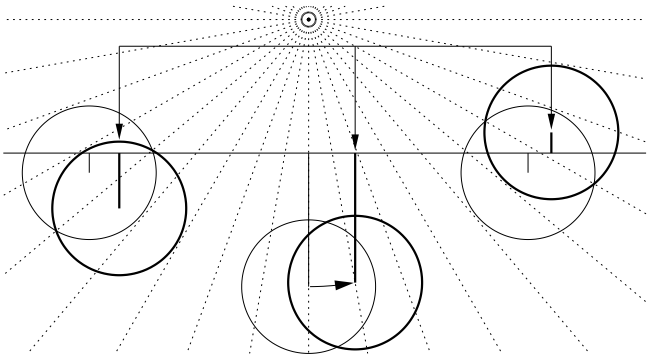

Figure 10. A cartoon showing that the backward misalignment (counterclockwise rotation around $\vec{\mu}$) of a symmetric system of circular beams results in the lag of the central component with respect to the centroid of the flanking pair. Thick lines present the misaligned case. The horizontal line marks the path of the sightline.

5.1 Centroid shift due to the asymmetric location of the beam system

Since the pulsars considered by GG03 exhibit approximate symmetry of their profiles, we consider a beam system which is perfectly symmetric with respect to the central plane ($\phi_{m,0}$-plane) of its central stream. To emulate the asymmetry, the beam system is rotated by a small angle ϵ with respect to the MM. Such a system with five identical beams is presented in Fig. 9. Consecutive circles along each beam again present the fixed-intensity contours at different and equally separated ν. All the contours are also equally separated in θ, ie. the θ spectral gradient is assumed to be the same for all beams. The misalignment of the system with respect to the MM produces a lag of the central component with respect to the centroids of the flanking pairs. This is because in the considered case (flat geometry with $\alpha \sim 90^\circ$) the observed pulse longitude of a component is given by:

$$\phi = \theta_\nu \sin\phi_m \tag{1}$$

where the angle $\theta_\nu \equiv \theta(\nu)$ corresponds to the fixed-intensity contour at the observed frequency ν, (hereafter the index ν will be omitted), and ϕ_m is the azimuth of the stream (note that ϕ_m is negative on the LS and positive on the TS). If the same-ν contours in different beams are located at the same θ, the slower-than-linear increase of $\sin\phi_m$ ensures that the LS spaces between adjacent components are larger than the 'corresponding' TS spaces (Fig. 10).

A simple mathematical model, presented in the next subsection (5.1.1) reveals that the properties of the model shown in Fig. 9 are consistent with the observed ν-dependent characteristics of the centroid shift. The model can simultaneously explain the normal apparent RFM, the sign (direction) of the shift, the increase of the shift with decreasing ν, and the increase of the shift towards the profile periphery.

However, the misalignment of the beam system has no built-in preference for the *leftward* shift of the centroids. A mirror image of Fig. 9 would produce exactly the opposite effect – the lag of the centroids with respect to the central component. Moreover, the effect must be affected by the AR shift, as soon as there are altitude differences associated with detectable parts of different streams (see Sect. 5.2).

5.1.1 *Simple model for the accidental shift of centroids*

The mathematical model presented in this section assumes the circular fixed-ν patterns shown in Fig. 9, ie. the case shown in Fig. 3b is modelled with the case shown in Fig. 3a. We can define an intra-system magnetic azimuth Φ measured around $\vec{\mu}$ from the central beam of Fig. 9, so that $\phi_m = \Phi + \epsilon$. The beam system is symmetric in Φ. The longitudes of the LS and TS components then become: $\phi_L = \theta\sin(-|\Phi_L| + \epsilon)$ and $\phi_T = \theta\sin(\Phi_T + \epsilon)$, respectively. The LS azimuth is assumed to be negative, so we use the absolute value to expose the magnitude of ϕ. For our perfectly symmetric beam system $|\Phi_L| = \Phi_T = \Phi$. The location of a pair centroid is then

$$\phi_{\rm pair} = \frac{\phi_L + \phi_T}{2} = \theta\cos\Phi\sin\epsilon. \tag{2}$$

The central component ('core') is located at the pulse phase

$$\phi_{\rm ctc} = \theta\sin\epsilon. \tag{3}$$

Assuming the same $\theta(\nu)$ for both the central and flanking components, the centroid precedes the 'core' by the pulse phase interval

$$\Delta\phi_{\rm obs} = \phi_{\rm pair} - \phi_{\rm ctc} = \theta\sin\epsilon(\cos\Phi - 1) \ < \ 0. \tag{4}$$

For pairs of more peripheric components at a larger Φ (smaller $\cos\Phi$) the magnitude of $|\Delta\phi_{\rm obs}|$ increases and so the lag of the central component. This is consistent with the properties of pulsars studied by Gupta and Gangadhara. The lag increases with the misalignment ϵ of the beam system (eq. 4).

Thus, for a bunch of similar beams with similar angular spectral gradient in the θ-direction, the misalignment alone can produce the forward shift of centroids, which is larger for the outer pairs of components. However, GG03 also show that in the observed profiles the flanking pairs of components precede the 'core' by a phase interval which increases with decreasing ν. To test if the 'accidental asymmetry' model of Fig. 9 can explain this, we will use the following simple mathematical model.

With the flat and equatorial approximation (small beam, $\alpha \approx 90^\circ$), The observed pulse longitude of a peak of a component is moving with the frequency at a rate:

$$\frac{d\phi}{d\nu} = \frac{d\phi}{d\theta}\frac{d\theta}{d\nu} = \frac{d\phi}{d\theta}\Delta^\theta_{\rm sp} = \Delta^\theta_{\rm sp}\sin(\phi_m) \tag{5}$$

where $\Delta^\theta_{\rm sp} = d\theta/d\nu$ sets the angular scale of spectral variation which corresponds to the displacement of the fixed-ν contours in the θ direction.[7] In general, $\Delta^\theta_{\rm sp}$ may change along the beam and can be different for beams located at different ϕ_m.

Below we consider the negative of derivative (5) to learn how the profiles evolve with decreasing frequency ($-d\nu = \nu_{\rm low} - \nu_{\rm high}$). Accordingly, with *decreasing* frequency, the central component moves rightward at the rate:

$$v_{\rm ctc} = \frac{d\phi_{\rm ctc}}{-d\nu} = -\frac{d\phi_{\rm ctc}}{d\theta}\Delta^\theta_{\rm sp} = \Delta^{\rm ctc}\sin\epsilon \approx \Delta^{\rm ctc}\epsilon \tag{6}$$

[7] Note that if $\Delta^\theta_{\rm sp}$ is considered as a free parameter, then the mathematical model is valid for any fixed-ν patterns, for which $d\phi/d\nu \propto d\phi/d\theta$.

where the index 'ctc' stands for the 'central component', and we have substituted $\Delta^{\theta}_{\rm sp} = -\Delta^{\rm ctc}$ for the θ spectral scale of the central component. The minus sign is supposed to reflect the normal RFM, for which $d\theta/d\nu < 0$ and $\Delta^{\rm ctc} > 0$. For a pair of flanking components (inner or outer) we have $d\phi/d\theta = \sin(\Phi_i + \epsilon)$, where the index '$i$' refers either to the leading ($i = L$) or trailing ($i = T$) location with respect to the central beam. Therefore, the speeds at which the components on the LS and TS departure from the MM at *decreasing* frequency are:

$$v_{L} = \frac{d\phi_{L}}{-d\nu} = \Delta^{L} \sin(-|\Phi_{L}| + \epsilon) \tag{7}$$

$$v_{T} = \frac{d\phi_{T}}{-d\nu} = \Delta^{T} \sin(\Phi_{T} + \epsilon), \tag{8}$$

where Δ^{L} and Δ^{T} set angular the spectral scales for the corresponding flanking components, ie. $d\theta_i/d\nu = -\Delta^{i}$. For the symmetric properties of the beam system ($|\Phi_{L}| = \Phi_{T} = \Phi$, $\Delta^{L} = \Delta^{T} = \Delta^{\rm pair}$, Fig. 9), the pair's centroid moves rightward at the speed

$$v_{\rm pair} = \frac{v_{L} + v_{T}}{2} = \Delta^{\rm pair} \sin\epsilon \cos\Phi \approx \Delta^{\rm pair} \epsilon \cos\Phi. \tag{9}$$

If the spectral properties of the central and flanking subbeams are the same ($\Delta^{\rm ctc} = \Delta^{\rm pair}$), the rightward speed of the centroid is smaller than the speed (6) of the central component, and the more so for more peripheral pairs. Therefore, the 'core' lag increases with decreasing observation frequency (or, more precisely, with increasing θ), in agreement with the afore-mentioned observations. The rate at which the centroid departures from the core is:

$$v_{\rm obs} = v_{\rm pair} - v_{\rm ctc} = -\sin\epsilon(\Delta^{\rm ctc} - \Delta^{\rm pair}\cos\Phi). \tag{10}$$

Since the rightward speed of a pair centroid (eq. 9) decreases towards the profile periphery, the centroids of more peripheral pairs departure from the core at a larger rate. This behaviour is consistent with observations.

Accordingly, the backward misalignment of the beam system, shown in Fig. 9, can simultaneously explain all the ν-dependent features identified for the pulsars of Gupta and Gangadhara: 1) the normal apparent RFM, 2) the lag of the central component, 3) the increase of the lag with decreasing ν, and 4) the increase of the lag for more peripheric pairs.

In general, the θ spectral scale may depend on θ and be different for different subbeams. As demonstrated by eq. (10), the difference between $\Delta^{\rm ctc}$ and $\Delta^{\rm pair}$ at the sightline crossing points can change the magnitude and direction of the centroid shift. For example, for some physical reasons the θ spectral scale could increase with the azimuth ϕ_m in a slightly asymmetric way with respect to the MM. This could produce a result identical to that in Fig. 9 even for a symmetric beam system centred at the MM. However, such spectrally-based interpretations do not have an obvious shift-sign preference and fail to automatically justify the increase of the shift towards the periphery of a profile (at a fixed ν) as well as the increase of the shifts with ν.

The number of possible combinations of parameters (different shape of the fixed-ν pattern, direction of the misalignment, and the sign of spatial RFM) is larger than discussed above, and they result in different observable properties. For instance, if the system of circular patterns is misaligned leftward with respect to the MM (opposite than shown in Fig. 9), then the pair centroid lags the central component by a phase interval increasing with Φ (eq. 4 with a negative ϵ). For decreasing ν, such a centroid would departure rightward from the 'core' (for a negative ϵ, eq. 10 predicts $v_{\rm obs} > 0$).

For the elongated patterns of Figs. 5 and 3c (with little or no apparent RFM), the location of components is determined by the points at which the sightline is crossing through the central azimuth of the beam (eq. A1). As we show in the Appendix, a system of such elongated beams would have to be misaligned leftwards (opposite than shown in Fig. 9) to produce the centroid advance. This type of a model (with no apparent RFM) would exhibit a frequency-independent lag of the central component.

The accidental asymmetry model shown in Fig. 9 is then consistent with the properties of pulsars described by GG03. However, depending on the direction of the beam misalignment (the sign of ϵ), it can produce both the leftward and rightward shifts. This may possibly be inconsistent with the fact that pulsar literature is dominated by descriptions of the leftward centroid shifts that increase with decreasing ν and with the proximity of profile periphery. However, the rotation of a pulsar, through the AR effects, is able to induce both the system's spatial asymmetry in $\delta_{\rm cut}$ as well as some ϕ_m-asymmetry in the system's spectral gradient. Therefore, we turn now to the subject of how pulsar rotation breaks the symmetry of the multiple-stream system through the AR effects.

5.2 Shift of the centroids due to the AR effects

Fig. 11a presents the sky-projected beam that should be typical for the M pulsars. The perfect symmetry is assumed only to clearly expose the phenomenon of the centroid shift. In general, we allow for a variety of asymmetries (in ϕ_m, $\Delta\phi_m$, and θ, see Fig. 18 in DRD10 and the illustrations of beams in Wang et al. 2014). However, the low-altitude dipolar magnetic field, as well as the electric field within the polar tube, are expected to be symmetric with respect to the MM. Therefore, it is natural to assume that the left-right symmetry should be on average found in pulsars. However, the AR-induced shift of centroids is expected to appear also for beam systems which are misaligned with respect to the MM.

The elliptic contours in Fig. 11a present the fixed-ν intensity pattern in the way similar to Fig. 2. The ellipses mark the uniform θ spectral gradient. In reality they may be more elongated in the direction of the stream (see Figs. 5 and 3bc), but this would make the figure unclear. Emission at a fixed ν is not constrained to the interior of an ellipse only. The ellipses may present, let us say, the 90% intensity level, with the peak emissivity at the centre of each ellipse. The solid horizontal marks the passage of the line of sight, again for a large dipole inclination and an overall small angular extent of the beam (which allows us for the flat approxiation of a generally-spherical case).

The pulsars that exhibit the centroid shift also show the normal apparent RFM. The separation of their outer peaks increases with decreasing frequency. Simultaneously, the centroid shift becomes larger and the more so for the outer pair of components (GG01). As has been shown in Sect. 4, for pulsars exhibiting the normal apparent RFM,

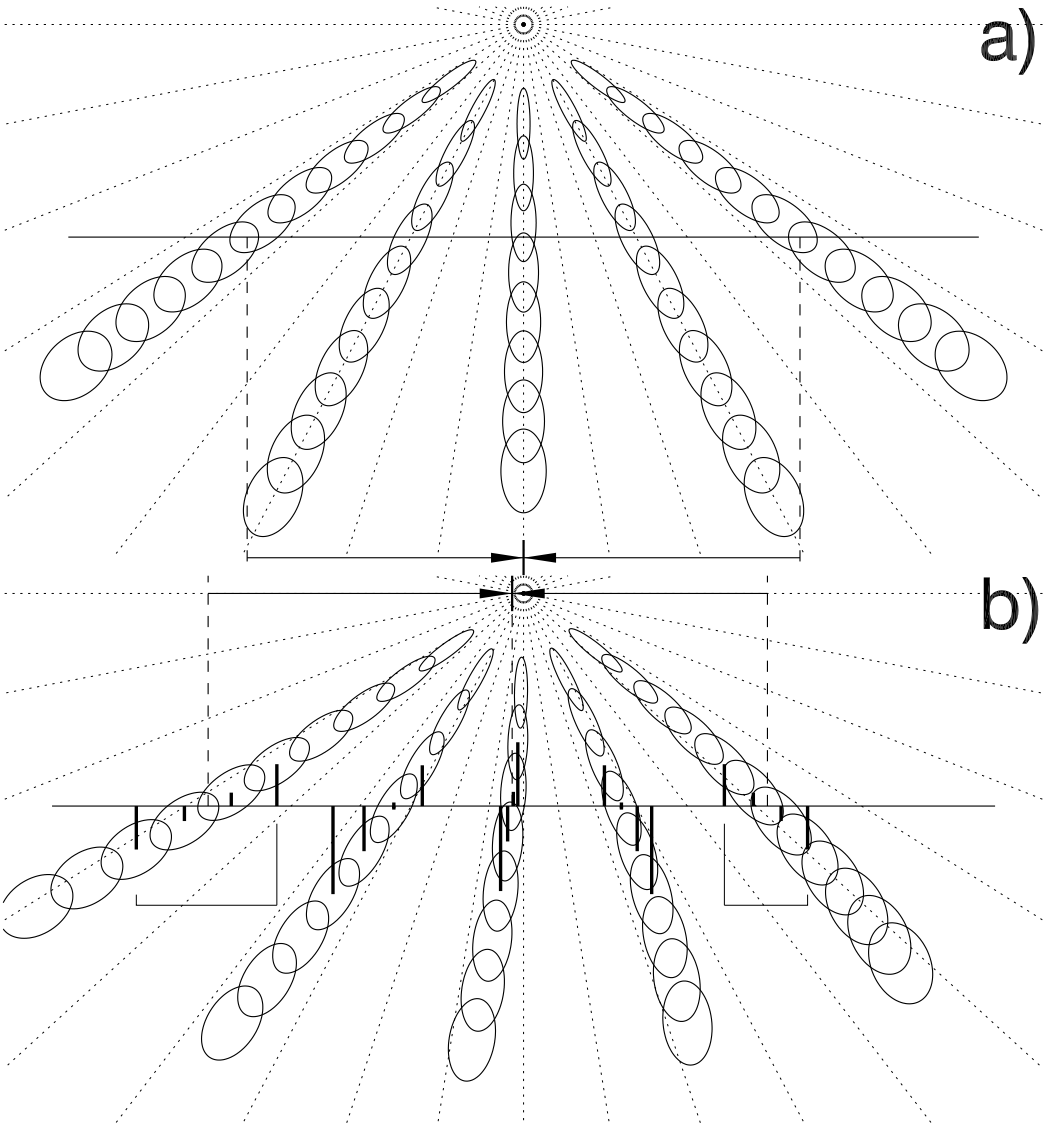

Figure 11. The mechanism of central component's lag with respect to centroids of outer components. **a)** A sky-projected emission beam with no aberration-retardation effects included. The ellipses present fixed-intensity contours at different frequencies, which decrease outwards. Emission altitude decreases towards the dipole axis. **b)** The beam with the AR-effects included. Note the forward bending of the individual beams. All ellipses were shifted leftward by a θ-dependent interval $|\Delta\phi| \propto r \propto \theta^2$. The lag of the central component is marked with the horizontal arrows. Note the decreased cut angle $\delta_{\rm cut}$ and the increased width of the leading components. This smaller value of the leading-side-$\delta_{\rm cut}$ implies a larger lag at lower ν, through the mechanism shown in Fig. 2. The ellipses on the TS are more overlapping with each other, which enhances the effect of the centroid shift.

the altitude of emission region must increase steeply with decreasing ν. The frequency associated with different ellipses in Fig. 11 is then decreasing with the angular distance from the dipole axis.

Since circumpolar B-field lines are quasi-radial, all the fixed-ν ellipses undergo the leftward AR shift (in the direction of early rotational phase) by $2r/R_{lc}$, irrespective of the dipole tilt α (Dyks et al. 2004). This is shown in Fig. 11b, in which the streams are bent in the direction of rotation. In a dipolar field the radial distance of emission r increases with the angular distance θ from the dipole axis according to $r \propto \theta^2$ so the magnitude of the shift quickly increases along the beam. Therefore, the central component is shifted leftward by the smallest interval of pulse longitude, because the sightline cuts the 'core stream' at the smallest θ and r. The inner pair of components undergoes a larger shift, but not as large as the outer pair. A result of a full 3D simulation of this effect is presented in Fig. 4 of DR12.[8]

As can be seen in Fig. 11b, the AR effects break the beam symmetry in such a way that the cut angle $\delta_{\rm cut}$ decreases on the LS whereas it increases on the TS. This has

[8] Note that the most vertical streams in Fig. 4 of DR12 correspond to $\phi_m = 170^\circ$ (the top one) and $\phi_m = 10^\circ$ (the bottom one), ie. the 'core beam' (corresponding to the stream within the MM) has been replaced with a second neighbouring beam of a stream located on the TS.

several consequences: 1) As shown with the horizontal arrows, the central component ('core') lags the centroids of pairs of outer components. 2) The leading components become wider than the trailing ones (see Ahmadi and Gangadhara 2002, and Dyks et al. 2010b for observational evidence). 3) Because $\delta_{\rm cut}$ is smaller on the LS, for decreasing ν the leading components departure from the 'core' faster than the trailing components. This is marked with the short thick bars that connect the centres of fixed-ν ellipses with the sightline path.[9] Fig. 4 in GG01 presents the observed version of this effect. 4) The angular distance θ from the sky-projected, low-altitude dipole axis becomes larger for the leading components, than for the 'corresponding' components on the TS. This contributes to the left-right asymmetry of the profile, because the LS patterns become more spread on the sky, so the peak flux of a leading component decreases in comparison to a 'corresponding' trailing component. This effect should be strongest for fast rotators, and may be responsible for the ubiquitous weakness of the LS in main pulses of MSPs (see eg. Fig. 2 in DRD10; Demorest 2007). Thus the extension of the LS emission over a long stretch of pulse longitude occurs also in the stream model, along with the simultaneous pile up of emission on the TS (see. Dyks et al. 2010b). 5) Since the consecutive ellipses in the trailingmost stream are more overlapping with each other, the spectrum is more broadband on the TS. This enhances the asymmetry of components' shifts thereby increasing the centroid shift.[10] Thus, the AR-induced asymmetry does not only generate the shift through the asymmetry of $\delta_{\rm cut}$. It may also make the TS spectrum more broadband, increasing the disproportion of the shifts on the LS and TS. [11]

Because of the spectral gradient asymmetry, the trailingmost component should have a broader spectrum, ie. extending over a wider range of ν, than the leadingmost component. The TS of a main pulse should then exhibit weaker shape evolution with ν than the trailing side, as observed eg. for PSR J1012+5307 (Dyks et al. 2010b).

[9] Note that the bars do not mark the observed peak positions of fixed-ν components, as was the case in Fig. 2, because the elliptic shape of the intensity decline (Fig. 3b) is ignored to maintain the clarity of Fig. 11. This is a technical detail which does not change our conclusions qualitatively. The faster departure of the LS components also exists for circular patterns (Fig. 9), which were not used in Fig. 11 to make it look more realistic.

[10] This can be understood as follows: Let us assume that a fixed frequency interval, say between 0.4 GHz and 1.4 GHz, corresponds to the transition from one elliptic contour to the adjacent one. For a more broadband spectrum (more overlapping ellipses on the TS), the angular displacement (measured along the beam) of a 0.4-GHz contour from a 1.4-GHz contour is smaller. Hence the shift of the trailing component is smaller than that of the leading one, for which the spectrum is less broadband (less overlapping ellipses).

[11] Physically, the stretched angular distance between the leading component and the dipole axis, corresponds to the larger curvature of electron trajectories on the LS (see Fig. 2 in Dyks et al. 2010b; Thomas et al. 2010).

5.2.1 Simple model for the AR-induced shift of centroids

As in Sect. 5.1.1, we model the intermediate case of Fig. 3b with the circular patterns of Fig. 3a. The pulse longitude of a component is given by

$$\phi = \phi' + \Delta\phi_{AR} = \theta \sin\phi_m - k\theta^2, \tag{11}$$

where ϕ' represents the pulse longitude observed for a beam with no AR effects included (Fig. 11a, eq. 1), and the AR shift is equal to

$$\Delta\phi_{AR} = -2\frac{r}{R_{lc}} = -\frac{8}{9}\frac{\theta^2}{s^2} = -k\theta^2, \tag{12}$$

where $k = 8/(9s^2)$, and $s = \theta_m/(r/R_{lc})^{1/2}$ is the footprint parameter (eg. Arons 1983). In the case of a non-orthogonal dipole inclination α, the first term of eq. (11) (but not the second one) should be rescaled roughly by a factor $1/\sin\alpha$ but this effect is ignored because it is symmetric in ϕ_m. The observed pulse longitude of a component changes with decreasing frequency at the rate of

$$-\frac{d\phi}{d\nu} = -\frac{d\phi}{d\theta}\Delta^{\theta}_{\rm sp} = -\Delta^{\theta}_{\rm sp}\left(\sin\phi_m - 2k\theta\right). \tag{13}$$

As before, the negative derivative is considered to learn how the profiles evolve with decreasing frequency. The central component ($\phi_m = 0$) therefore moves leftward at the 'spectral speed'

$$v_{\rm ctc} = -\frac{d\phi_{\rm ctc}}{d\theta}\Delta^{\theta}_{\rm sp} = -2k\Delta^{\rm ctc}\theta_{\rm ctc}, \tag{14}$$

where $\theta_{\rm ctc}$ is the magnetic colatitude of the propagation direction for the point at which the line of sight is passing through the 'core'. The angular scales of spectral variations for different components are determined as in Sect. 5.1.1, ie. $\Delta^{\theta}_{\rm sp} = -\Delta^{\rm ctc}$, $\Delta^{\theta}_{\rm sp} = -\Delta^{L}$, etc. For a pair of flanking components at magnetic azimuths ϕ^L_m and ϕ^T_m we have $d\phi_i/d\theta = \sin\phi^i_m - 2k\theta_i$, where $i = L$ or T, so their leftward speeds across a profile are:

$$v_L = -\frac{d\phi_L}{d\theta}\Delta^{\theta}_{\rm sp} = \Delta^{L}\left[\sin(-|\phi^L_m|) - 2k\theta_L\right] \tag{15}$$

$$v_T = -\frac{d\phi_T}{d\theta}\Delta^{\theta}_{\rm sp} = \Delta^{T}\left[\sin(\phi^T_m) - 2k\theta_T\right] \tag{16}$$

In the case of the symmetric properties of the stream system with respect to the MM ($\phi^L_m = \phi^T_m = \phi^{\rm pair}_m$, $\theta_L = \theta_T = \theta_{\rm pair}$, $\Delta^L = \Delta^T = \Delta^{\rm pair}$), the centroid moves leftward at the speed:

$$v_{\rm pair} = \frac{v_L + v_T}{2} = -2k\Delta^{\rm pair}\theta_{\rm pair}, \tag{17}$$

where $\theta_{\rm pair}$ is the θ-angle for the locations of the sightline-cut through the flanking streams. In agreement with the expectations based on Fig. 11, for $\Delta^{\rm ctc} = \Delta^{\rm pair}$ the centroid speed is larger than the 'core' speed $v_{\rm ctc}$, because at the locations probed by the line of sight $\theta_{\rm ctc} < \theta_{\rm pair}$. The observed ν-dependent speed at which the centroid moves with respect to the central component is given by:

$$\begin{aligned} v_{\rm obs} &= v_{\rm pair} - v_{\rm ctc} = -2k\Delta^{\rm pair}\theta_{\rm pair} + 2k\Delta^{\rm ctc}\theta_{\rm ctc} = \\ &= -2k(\Delta^{\rm pair}\theta_{\rm pair} - \Delta^{\rm ctc}\beta), \end{aligned} \tag{18}$$

Eq. (18) has the required property of producing larger shift of centroid for the more peripheral (outer) pairs of components (which have larger θ at the sightline-crossing points). Moreover, the shift increases with decreasing ν, because $v_{\rm obs} \propto \theta$ and $d\theta/d\nu < 0$ for the pulsars analysed in

GG03. The AR effect can thus generate all the observed ν-dependent effects exhibited by these pulsars. In contrast to the accidental shift caused by the beam-system misalignment, the AR effects displace the centroid in only one direction (leftward, provided r is smaller for inner components). The AR shift can therefore be either enhanced or made weaker by the misalignment. If locations of streams in pulsars are accidental, in most cases the central component should lag the centroids. The opposite arrangement (lag of the centroid) can occur only for objects in which the misalignment dominates over the AR effects.

The widely-used method of r-determination from the 'core' lag needs to be reconsidered in view of the stream interpretation. If the streams in the corotating pulsar magnetosphere are so symmetric as shown in Fig. 11a, then, from eq. (11), the 'core' lag is equal to:

$$\begin{aligned}\Delta\phi_{\rm obs} &= \phi_{\rm pair}-\phi_{\rm ctc} = -k\theta^2_{\rm pair}+k\theta^2_{\rm ctc} = \\ &= -k(\theta^2_{\rm pair}-\beta^2) = -2\left(\frac{r_{\rm pair}}{R_{lc}}-\frac{r_{\rm ctc}}{R_{lc}}\right) \qquad (19)\end{aligned}$$

Thus, the published emission altitudes that were derived within the conal model may still represent the altitude differences between the 'core' component and the flanking components. This is because it does not matter whether the AR-shifted patches of intensity are fragments of a single cone or fragments of two symmetric streams. What has changed is the interpetation of the altitude – it now represents the altitude of that part of a stream that happened to be probed by our line of sight. The 'core' altitude, eg., represents the altitude of the sightline-crossing point – it does not have to be next to the neutron star surface.

It needs to be emhasized that the AR-induced lag of 'core' is a robust effect which operates also for not perfectly symmetric system of streams. In the asymmetric case shown in Fig. 9, the AR effects would also bend the streams forward. The components would accordingly move forward in phase, enhancing the 'core' lag that results from the misalignment alone. In the case of the leftward misalignment of the beam system (negative ϵ) the AR effects could possibly lead to the 'core' lag, provided they were stronger than the effects of the misalignment, which occurs roughly for $\epsilon<\theta$. The magnitude of the AR shift quickly increases with θ so the AR-induced 'core' lag is likely to appear also for systems of streams which are not fully symmetric with respect to the MM.

However, the fact that the *magnitude* of the centroid shift can be affected by *any* asymmetry of the type shown in Fig. 9, makes the altitudes obtained with the AR-lag method less reliable. Direct use of eq. (19) is risky, because it assumes perfect symmetry of the stream system and ignores spectral differences between the streams (eg. one may have $\theta_L(\nu)\neq\theta_T(\nu)$ for the flanking streams). In the case of the intrinsically asymmetric beam structure, results of Sect. 5.1 need to be convolved with the AR lag.

Therefore, whereas the AR-induced lag can be observed also for the intrinsically non-symmetric geometry, eq. (19) is valid only for the fully symmetric case.

We conclude that the AR effects working within streams with spatial spectral gradient (spatial RFM) explain both the broken symmetry of profiles, as well as the increasing strength of this effect with decreasing frequency. We emphasize that in the stream model the low altitude of the 'core' is not an ad-hoc assumption made to produce the observed centroid shift. In the stream model the low-r location of 'core' naturally results from the dipolar geometry of streams, which near the dipole axis (small θ) occupy small r. In the case of the inner components (associated with more meridional streams) the line of sight cuts through the streams at a smaller angle θ and smaller r, provided the streams have similar s.

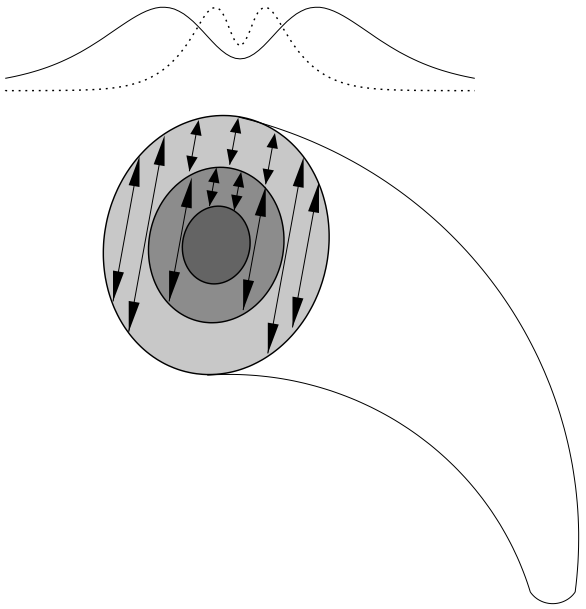

Figure 12. The cross-section through a magnetospheric stream, exposing the transverse decline of plasma density (grey contours). The arrows show that the sightline-integrated emissivity is larger at the azimuthal sides of the stream. Moreover, the emission from the bottom part of the stream can be obscured by the central high-density region. The resulting pulse profiles are shown on top. The dotted one is for a larger ν.

We have discussed only the simplest case of identical streams located at different azimuth ϕ_m. A much larger variety of streams (with different s, r, θ_m, $\Delta^\theta_{\rm sp}$, and azimuthal widths and separations) apparently exist in magnetospheres of real pulsars. This would explain the diversity of observed properties of pulsar profiles.

6 OBSCURATION EFFECTS AND BIFURCATED EMISSION COMPONENTS

In the cone/core scenario the radio emission was believed to originate from well-separated and narrow intervals of altitude and footprint parameter. This was not likely to lead to obscuration effects.

In the case of elongated streams, the geometry that leads to eclipses of lower-r emission can appear in at least two cases. First, this happens when a laterally extended, quasi-uniform emission is blocked from our view by a dense non-emitting stream. This case was shown to produce deep double notches in the profiles of both normal and millisecond pulsars (DRD10; DR12; McLaughlin & Rankin 2004).

Second, when the central high-density region of the stream extends sufficiently far in the longitudinal direction, the bottom parts of the stream, located on its concave side, can also be eclipsed (ie. the radiation from this region can be scattered or absorbed and dissipated). This can be seen in Fig. 6, in which the lowermost 'ray', emitted near the bottom of the lower emission region, must cross the full thickness of the region before reaching the outer low-density regions. Depending on the transverse gradient of plasma density in the stream, and on the observed frequency, the ray can be obscured. This can diminish the flux observed at the centre of a component, producing a bifurcated emission component (BEC), similar to those observed in PSR J0437−4715 and J1012+5307. Moreover, the tubular shape of transverse density pattern (Fig. 12) should additionally enhance the flux in the azimuthally-outer parts of the associated component. This is because the radio emission occurs within the planes of fixed magnetic azimuth ϕ_m (if the extent of the $1/\gamma$ microbeam is negligible). Crossections of the stream with these fixed ϕ_m planes are shown with the arrows in Fig. 12. Different zones of equal density are shown with different grades of grey. Since the radio emission occurs in the planes containing the arrows and the dipole axis, the largest emissivity per steradian corresponds to the azimuthal sides of the stream. Thus a 'limb brightening' can be expected. Emission at a larger frequency originates from the inner regions of the stream (the inner ring in Fig. 12) which implies the narrowing of BECs with frequency, consistent with the observations of PSR J0437−4715 and J1012+5307. Thus, the nature of BECs may be macroscopic, and not related to the microphysical (elementary) emission beam. This would solve the problem of large energetic requirements implied by the microscopic interpretation (Dyks & Rudak 2013; Gil & Melikidze 2010). However, it is less clear why the BECs should have so high symmetry as observed, because rotation tends to remove the stream away from the path of a to-be-eclipsed ray. It is also important to note that in the superstrong magnetic field only the radiation in the ordinary polarisation mode would be eclipsed. The extraordinary polarisation mode, however, is not emitted within the ϕ_m-plane anyway (DRD10; Gil et al. 2004). The mode-dependent obscuration would introduce imbalance between the observed contribution of orthogonal polarisation modes, which should change with the distance from a BEC's centre.

It is also possible that both factors (micro- and macroscopic) shape the BECs. Regardless of this issue, the general interpretation of the BECs in MSPs remains similar to the one described in DRD10 and DR12: they are caused by the broad-band, locally-bidirectional[12] radio emission, and are observed when our line of sight passes through streams in pulsar magnetosphere. The only difference is that in the macroscopic case, the quasi-local bifurcation is attributed to the opacity of a segment of a narrow stream.

With the possibility of the macroscopically-generated, locally-bidirectional beams, one needs to ask if double notches can also be created by obscuration of these macroscopic bifurcated beams. This does not seem to be possible, because the emitter associated with the phenomenon of double notches (see Fig. 12 in DRD10) has to be extended in two dimensions (azimuth and latitude) to be consistent with the quasi-isotropic radio emission in which double notches are observed. The emitter does not have the geometry of the stream shown in Fig. 12. Moreover, the notches are well-fitted with the curvature radiation microbeam (Fig. 6 in DR12), have different shapes than BECs (Sect. 3.3 in DR12), and all of them are narrower than the problematic BEC of PSR J1012+5307 (see Fig. 4 in Dyks & Rudak 2013). Therefore, the microscopic nature of double notches continues to present a promising model.

[12] 'Bidirectional' means the emission into the lobes of the bifurcated beam shown in Fig. 1 of DR12. It does not mean the emission in two opposite directions.

7 CONCLUSIONS

We have shown that the main frequency-dependent phenomena exhibited by radio pulsar profiles: the apparent RFM and the frequency-dependent centroid shift can be naturally explained within the stream model – the model which assumes fan-shaped radiation beams produced by streams flowing in pulsar magnetosphere.

By considering the spatial spectral gradient along the stream, we have shown that even some detailed aspects of the phenomena can be effortlessly reproduced by the stream model. These include the weaker apparent RFM of the inner 'conal' pair, as well as the increasingly large centroid shift at lower frequencies. The weak spreading of inner pair components is a trivial consequence of more orthogonal stream cutting. In the stream model, the shift of centroids does not require the complicated and arbitrary positioning of the core, inner cone and outer cone emission at disparate altitudes and magnetic colatitudes. Instead, the altitude differences result naturally from the geometry of the cut itself.

Surprisingly the shifts of centroids of both signs can appear even with no altitude differences (and no AR affects) associated with the fan beam. However, only the backward misalignment of the beam system has the properties consistent with pulsars described in GG01 and GG03. Whenever both the shift-inducing conditions exist, ie. when the symmetric system of beams is misaligned and emission altitude increases towards the periphery of the beam, then the AR shift can be enhanced, diminished or reversed by the effects of the misalignment. In contrast to the misalignment shift, the AR shift always provides the type (sign) of the asymmetry and the frequency behaviour which is observed for pulsars described by GG03. This naturally results from the geometry of streams which in the dipolar field occupy low altitudes at small θ.

In the case of the stream model, even for identical locations of the streams on their corresponding planes of fixed magnetic azimuth (same Δs, Δr), the approximate left-right symmetry of profile properties is likely to appear because smaller altitudes are sampled for inner (more meridional) streams. The 'core' component is created by the sightline cut through a near-meridional stream whereby the lowest altitudes are probed. The altitude differences required to produce the centroid shift ensue naturally, because the line of sight picks up a lower-altitude emission in the middle of the profile, ie. no radial displacements need to be introduced between different streams to generate the AR lag of the central component (though in general such differences in r are

not excluded). The stream model can also explain some differences between the frequency-dependent behaviour of normal pulsars and MSPs.

It has been shown that by introducing the azimuthal non-uniformity to the pulsar beam one can avoid several problems which remain challenging for the conal model. In particular, the problem of origin of the 'core' component in the conal model disappears, with the role of the physical core region taken over by the central stream. Interestingly, the observed 'core' emission is still found to originate from the lowest altitudes and this is probably why its properties are sometimes observed to be different from properties of the outer components.

Similar effects (decrease of r towards the centre of the profile) are likely responsible for the apparent symmetry of fluctuation spectra with respect to the centre of profiles (Backer 1970; Maan & Deshpande 2014). The origin of subpulse drift (eg. Weltevrede et al. 2007; Ruderman & Sutherland 1975), the apparent 'carousel circulation' (Deshpande & Rankin 2001) and other single-pulse effects certainly deserve a careful study within the stream model with azimuthally-structured average emission pattern. The new type of radio beam may also impact the population studies (Story et al. 2007) and the multiwavelength lightcurve fitting (Pierbattista et al. 2014; Venter et al. 2012; Romani & Watters 2010). The elongated beams also provide the flexibility that is needed to interpret profiles of difficult objects such as the Crab pulsar (Moffett & Hankins 1996) or PSR B1821−24 (Johnson et al. 2013; Knight et al. 2006).

The azimuthal structure calls for explanation itself. Results of this paper suggest that more efforts should be put into the understanding of the azimuthal nonuniformity of pulsar magnetosphere, instead of the radially-separated emission rings, which seemed to be justified by the 'core'-lag effect, or by the general applicability of the conal classification scheme.

The apparent RFM and the centroid shift were providing considerable support for the conal beam model. However, we have shown that these conal interpretations can be successfully replaced with the stream-based reasoning. Furthermore the stream model is able to explain even such 'peculiarities' as the bifurcated components and double notches, which makes it a very successfull tool to interpret radio pulsar beams.

The evidence for the stream model (or fan-beam model) is mounting steadily. As recently shown by Wang et al. (2014) the fan beam model is more successful in reproducing the observed statistics of profiles' width and flux than the conal model. In the upcoming paper (Pierbattista & Dyks, in preparation) we show that the statistics of component locations within the profiles with 4 and 5 components (Q and M class) is inconsistent with the nested cone model. Teixeira et al. (2014) show that probably the most symmetric example of the Q-type profile (J0631+1036, Zepka et al. 1996) is best explained by the multiple-stream model, which avoids several problems of the conal interpretation. All this development is additionally supported by the recent beam maps of precessing pulsars, including the feebly constrained but fairly suggestive map of J1906+0746. The difficulties in reproducing the beam maps of other precessing pulsars with the use of conal beams, are likely caused by application of inappropriate beam topology.

The stream model is then supported by variety of arguments, it is able to explain several pulsar features, and avoids several problems of the conal model. With no reserve we therefore advance the view that pulsars possess fan beams emitted by outflowing plasma streams, whereas the nested cone/core beams may well not exist.

ACKNOWLEDGMENTS

We thank Patrick Weltevrede for a careful review. The work presented in this paper was funded by the Polish National Science Centre grant DEC-2011/02/A/ST9/00256.

REFERENCES

Ahmadi P., Gangadhara R.T., 2002, ApJ, 566, 365
Arons J., 1983, ApJ, 266, 215
Arons J., & Scharlemann E.T., 1979, 231, 854
Backer, D.C., 1970, Nature, 228, 752
Burgay M., Possenti A., Manchester R.N., Kramer M., McLaughlin M.A., et al. 2005, ApJ, 624, L113
Clifton T., & Weisberg J.M., 2008, ApJ, 679, 687
Cordes J. M., 1978, ApJ, 222, 1006
Demorest P., 2007, PHD Thesis, Univ. of California, Berkeley
Deshpande A.A., & Rankin J.M., 2001, 322, 438
Desvignes, G., Kramer, M., Cognard, I., Kasian, L., van Leeuwen, J., Stairs, I., & Theureau G. 2013, Proc. IAU Symposium No. 291, ed. J. van Leeuwen, 199
Dyks J., & Rudak B., 2012, MNRAS, 420, 3403 (DR12)
Dyks J., & Rudak B., 2013, MNRAS, 434, 3061
Dyks J., Rudak B., & Demorest P., 2010a, MNRAS, 401, 1781 (DRD10)
Dyks J., Rudak B., & Harding A. K., 2004, ApJ 607, 939
Dyks J., Wright G.A.E., & Demorest P., 2010b, MNRAS, 405, 509
Gangadhara R. T., & Gupta Y., 2001, ApJ, 555, 31 (GG01)
Gil J., & Kijak J., 1993, A&A, 273, 563
Gil J.A., & Melikidze G.I., 2010, astro-ph/1005.0678
Gil J., Lyubarsky Y., & Melikidze G.I., 2004, ApJ, 600, 872
Gupta, Y., & Gangadhara, R.T. 2003, ApJ, 584, 418 (GG03)
Hankins, T.H., & Rankin, J.M., 2010, ApJ, 139, 168
Johnson, T.J., Guillemot, L., Kerr, M., Cognard, I., Ray, P.S., Wolff, M.T., Bégin, S., Janssen, G.H. 2013, ApJ, 778, 106
Karastergiou, A., & Johnston, S. 2007, MNRAS, 380, 1678
Knight, H.S., Bailes, M., Manchester, R.N., Ord, S.M. 2006, ApJ, 653, 580
Komesaroff, M.M. 1970, Nature, 225, 612
Kramer M., Wielebinski R., Jessner A., Gil J.A., & Seiradakis J.H., 1994, A&AS, 107, 515
Kramer M., 1998, ApJ, 509, 856
Kramer M., Xilouris K. M., Lorimer D., Doroshenko O., Jessner A., Wielebinski R., Wolszczan A., Camilo, F. 1998, ApJ, 501, 270
Kramer M., Lange C., Lorimer D., Backer D.C., Xilouris K. M., Jessner A., & Wielebinski R. 1999, ApJ, 526, 957
Kuzmin, A.D., & Losovsky, B.Ya., 2001, A&A, 368, 230
Lorimer D.R., Stairs I.H., Freire P.C., Cordes J.M., Camilo F., et al., 2006, ApJ, 640, 428

Lyne A.G., & Manchester, R. N., 1988, MNRAS, 234, 477
Maan, Y., & Deshpande, A.D., 2014, ApJ, accepted (astro-ph/1407.6368v1)
Malofeev, V.M., Gil, J. A., Jessner, A., Malov, I.F., Seiradakis, J.H., Sieber, W., Wielebinski, R. 1994, A&A, 285, 201
Manchester, R.N., 2012, Proc. Electromagnetic Radiation from Pulsars and Magnetars, eds. W. Lewandowski, O. Maron, & J. Kijak, San Francisco, ASP Conference Series 466, 61
Manchester, R. N., Kramer, M., Stairs, I. H., Burgay, M., Camilo, F., Hobbs, G. B., Lorimer, D. R., Lyne, A. G., et al. 2010, ApJ, 710, 1694
Maron, O., Kijak, J., & Wielebinski R., 2000, A&ASS, 147, 195
McLaughlin M. A., & Rankin J. M., 2004, MNRAS, 351, 808
Michel, F.C., 1987, ApJ, 322, 822
Mitra D., & Rankin J. M., 2002, ApJ, 577, 322
Moffett D.A., & Hankins, T.H., 1996, ApJ, 468, 779
Navarro J., Manchester R. N., Sandhu J. S., Kulkarni S.R., Bailes M., 1997, ApJ, 486, 1019
Perera, B. B. P., McLaughlin, M. A., Kramer, M., Stairs, I. H., Ferdman, R. D., Freire, P. C. C., Possenti, A., Breton, R. P., et al. 2010, ApJ, 721, 1193
Pierbattista, M., Harding, A. K., Grenier, I. A., Johnson, T. J., Caraveo, P. A., Kerr, M., Gonthier, P. L., 2014, A&A, submitted (astro-ph/1403.3849)
Rankin J.M., 1983, ApJ, 274, 333
Rankin J.M., 1990, ApJ, 352, 247
Rankin J.M., 1993, ApJ, 405, 285
Rankin J.M., & Rathnasree N., 1997, J. Astrophys. Astron., 18, 91
Romani R.W., & Watters K.P., 2010, ApJ, 714, 810
Ruderman M.A., Sutherland P.G. 1975, ApJ 196, 51
Story S.A., Gonthier P.L., Harding A.K., 2007, ApJ, 671, 713
Teixeira M. M., Rankin J. M., Wright G. A. E., & Dyks J., 2014, MNRAS, submitted
Thomas, R.M.C., Gupta, Y., & Gangadhara, R.T. 2010, MNRAS, 406, 1029
Venter C., Johnson T.J., Harding A.K., 2012, ApJ, 744, 34
Wang P.F., Lai D., & Han J.L., 2010, MNRAS, 403, 569
Wang P.F., Wang C., & Han J.L., 2012, MNRAS, 423, 2464
Wang, H.G., Pi, F.P., Zheng, X.P., Deng, C.L., Wen, S.Q., Ye, F., Guan, K.Y., Liu, Y. & Xu, L.Q, 2014, ApJ, 789, 73
Weisberg J.M., & Taylor J.H., 2002, ApJ, 576, 942
Weltevrede P., Stappers B.W., & Edwards R.T. B.W., 2007, A&A, 469, 607
Wright, G. A. E., 2003, MNRAS, 344, 1041
You, X.P., Hobbs, G., Coles, W. A., Manchester, R. N., Edwards, R., Bailes, M.; Sarkissian, J., Verbiest, J. P. W., MNRAS, 378, 493
Zepka,A., Cordes, J. M., Wasserman, I., & Lundgren, S. C. 1996, ApJ, 456, 305

APPENDIX A: CENTROID SHIFT FOR ELONGATED SUBBEAMS

In the case of the elongated and broad-band beams there is little or no apparent RFM, as illustrated in Fig. 3c. Longitudes of components are then determined by the cross-section of the sightline path with the azimuth of the fan beams:

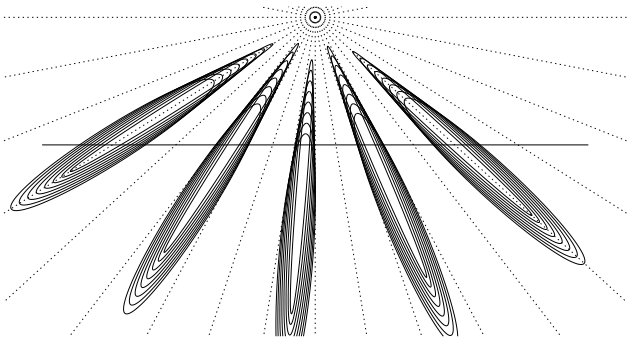

Figure A1. A system of beams misaligned with respect to the MM. The fan beams are elongated and spectrally nearly-uniform (a case with little or no apparent RFM). The horizontal marks the passage of the line of sight. Unlike in the case of the circular fixed-ν patterns (cf. Figs. 9 and 10) the lag of the central component appears for the leftward misalignment of the system.

$$\phi = \beta \tan \phi_m \tag{A1}$$

where β is the impact angle (Fig. 1). In contrast to the circular case discussed in Sect. 5.1.1 (see eq. 1), the observed pulse phase is now increasing with ϕ_m at a faster-than-linear rate of $\tan \phi_m$. Therefore, the LS spaces between adjacent components are larger than the 'corresponding' TS spaces, when the system is rotated leftward (Fig. A1), ie. in the opposite direction than in Fig. 9.

To calculate the centroid shift, we use the same intra-system magnetic azimuth Φ as defined in Sect. 5.1.1, ie. $\phi_m = \Phi + \epsilon$, where the misalignment angle ϵ is now negative. The longitudes of the LS and TS components then become: $\phi_L = \beta \tan(-|\Phi_L| - |\epsilon|)$ and $\phi_T = \beta \tan(\Phi_T - |\epsilon|)$, respectively. For a perfectly symmetric beam system $|\Phi_L| = \Phi_T = \Phi$. The location of a pair centroid is

$$\phi_{\rm pair} = \frac{\phi_L + \phi_T}{2} = \frac{\beta \tan\epsilon \, (1 + \tan^2 \Phi)}{1 - \tan^2 \Phi \tan^2 \epsilon}. \tag{A2}$$

Note that $\phi_{\rm pair} < 0$ since $\epsilon < 0$ for the misalignment shown in Fig. A1. The central component ('core') is located at the (negative) pulse phase

$$\phi_{\rm ctc} = \beta \tan \epsilon \tag{A3}$$

and lags the centroid by the pulse phase interval

$$\Delta\phi_{\rm obs} = \phi_{\rm pair} - \phi_{\rm ctc} = \frac{\beta \tan\epsilon \tan^2 \Phi (\tan^2 \epsilon + 1)}{1 - \tan^2 \Phi \tan^2 \epsilon}. \tag{A4}$$

The value of $\Delta\phi_{\rm obs}$ is negative, because $|\phi_{\rm pair}| > |\phi_{\rm ctc}|$ and $\epsilon < 0$. In the limit of small $|\epsilon|$ (and Φ not too close to 90°) the lag is equal to

$$\Delta\phi_{\rm obs} \approx \beta \tan\epsilon \tan^2 \Phi \tag{A5}$$

For small Φ (inner components located close to the central one) the centroid's location stays close to the position $\phi_{\rm ctc}$ of the central component. For increasing Φ (outer components) $\phi_{\rm pair}$ precedes the central component by a quickly increasing phase interval. The magnitude of the 'core' lag is then larger for the more peripheric pairs, in agreement with

the observations (GG01, GG03). The effect increases with the misalignment $|\epsilon|$ of the beam system (eq. A5).

Thus, for a bunch of similar, elongated beams with a broadband spectrum, the misalignment shown in Fig. A1 can produce the forward shift of centroids with respect to the MM. Moreover, the shift is larger for the outer pairs of components. However, in this case of the weak spectral variations, the lag should exhibit little or no dependence on frequency, and there should be no apparent RFM. The sign of the centroid shift would change (with the centroid following the central component) for the opposite misalignment than that of Fig. A1.